# Nuclear basket proteins regulate the distribution and mobility of nuclear pore complexes in budding yeast

Janka Zsok[1], Francois Simon[2], Göksu Bayrak[1], Luljeta Isaki[1], Nina Kerff[2], Amy Wolstenholme[1], Lucien E. Weiss[2]@, Elisa Dultz[1]@

[1]Institute of Biochemistry, ETH Zürich, Zurich, Switzerland

[2]Department of Engineering Physics, Polytechnique Montréal, Montréal, Québec, Canada

Correspondence to edultz@ethz.ch or lucien.weiss@polymtl.ca

## Abstract

Nuclear pore complexes (NPCs) mediate all traffic between the nucleus and the cytoplasm and are among the most stable protein assemblies in cells. Intriguingly, budding yeast cells carry two variants of NPCs which differ in the presence or absence of the nuclear basket proteins Mlp1, Mlp2 and Pml39. The binding of these basket proteins occurs very late in NPC assembly and Mlp-positive NPCs are excluded from the region of the nuclear envelope that borders the nucleolus.
Here, we use recombination-induced tag exchange (RITE) to investigate the stability of all the NPC subcomplexes within individual NPCs. We show that the nuclear basket proteins Mlp1, Mlp2 and Pml39 remain stably associated with NPCs through multiple cell-division cycles, and that Mlp1/2 are responsible for the exclusion of NPCs from the nucleolar territory. In addition, we demonstrate that binding of Nup2 also depletes Mlp-negative NPCs from this region by an independent pathway. We develope a method for single NPC tracking in budding yeast and observe that NPCs exhibit increased mobility in the absence of nuclear basket components. Our data suggest that the distribution of NPCs on the nucleus is governed by the interaction of nuclear basket proteins with the nuclear interior.

## Introduction

Nuclear pore complexes (NPCs) are large macromolecular assemblies that form channels in the nuclear envelope (NE) and mediate all transport between the nucleus and cytoplasm in eukaryotic cells (reviewed in Dultz et al., 2022; Petrovic et al., 2022). The NPC is composed of multiple copies of approximately 30 different proteins, termed nucleoporins (Nups). Its core consists of a stack of three rings with eight-fold rotational symmetry along the nucleocytoplasmic axis and two-fold symmetry along the NE axis. The outer rings, on both the nucleoplasmic and cytoplasmic side of the NPC, are decorated with asymmetrical appendages known as the nuclear basket and the cytoplasmic export platform, respectively (Figure 1A).

The nuclear basket is composed of three highly dynamic Nups carrying FG or FXF(G) domains (Nup1, Nup60 and Nup2) and three structural Nups (Pml39, Mlp1 and Mlp2), here collectively referred to as the basket filaments. The paralogues Mlp1 and Mlp2 are large proteins interspersed with coiled-coil regions that extend into the nucleoplasm, forming the main scaffold of the basket (Strambio-de-Castillia, Blobel, & Rout, 1999) (Figure 1B). They, along with Nup2, are recruited to the NPC by Nup60 via short linear interacting motifs (Cibulka, Bisaccia, Radisavljević, Carrillo, & Köhler, 2022; Dilworth et al., 2001). Pml39 binds to Mlp1 and to a lesser extent to Mlp2 and promotes the binding of additional copies of Mlp1 to the NPC (Gunkel, Iino, Krull, & Cordes, 2023).

While Nup1, Nup60 and Nup2 are found on all NPCs, the nuclear basket filaments are present only on a subset (Bensidoun, Reiter, Montpetit, Zenklusen, & Oeffinger, 2022; Galy et al., 2004; Benoît Palancade, Zuccolo, Loeillet, Nicolas, & Doye, 2005). This may be a consequence of their

extraordinarily late assembly: they bind to the NPC on average ~40 min after all other Nups have assembled (Onischenko et al., 2020). The mechanism of this late assembly is unclear, but mRNA metabolism may be required for basket assembly, since inhibiting transcription and mutating mRNA maturation factors involved in 3' end processing was recently found to result in defects in basket filament assembly (Bensidoun et al., 2022). Supporting this idea, Mlp-positive NPCs are normally not found in the region of the NE adjacent to the nucleolus (Galy et al., 2004), which is devoid of mRNA. Mutants that accumulate mRNA in the nucleolus no longer exclude Mlp-positive NPCs from the nucleolar region (Bensidoun et al., 2022). There is thus an intricate relationship between the nuclear basket filaments and RNA maturation and export. Indeed, in wild type cells, mRNA export and processing factors are specifically enriched at NPCs with nuclear basket filaments (Bensidoun et al., 2022), and the deletion of *PML39* or *MLP1* results in the leakage of unspliced RNAs into the cytoplasm suggesting that the nuclear basket plays a role in mRNA quality control (Galy et al., 2004; Benoît Palancade et al., 2005).

In addition to being involved in mRNA quality control, the nuclear basket filaments also contribute to genome protection by supporting DNA repair pathways and preventing R loops (García-Benítez, Gaillard, & Aguilera, 2017; Benoit Palancade et al., 2007). Intriguingly, a recent study showed that telomeric gene silencing is specifically carried out by NPCs without nuclear basket filaments (Kumar et al., 2023). This is not the only example of NPC specialization, and there is increasing evidence that different NPC compositional variants carry out specific roles in the cell (reviewed in Dultz et al., 2022). For example, components of the mRNA export machinery are lacking in NPCs of daughter cells, which delays their transition into S phase (Gomar-Alba et al., 2022). Also, replicatively aged yeast cells accumulate NPCs that lack components of the cytoplasmic export platform and the nuclear basket, thereby contributing to ageing (Meinema et al., 2022). The study of such variant NPCs is severely limited by average-based bulk methods, since they fail to capture the compositional heterogeneity in different complexes. Thus, methods that can distinguish between NPC subtypes and provide spatial and temporal resolution of single NPCs are required.

In this work, we develop recombination-induced tag exchange (RITE) into a system that allows us to track individual NPCs and to follow them through multiple cell cycles. We use this to systematically analyse the binding stability of Nups from all NPC subcomplexes in yeast. We show that Mlp1, Mlp2 and Pml39 are stably associated with NPCs through multiple cell cycles. Furthermore, we identify two pathways that reduce the density of NPCs in the nucleolar territory: First, binding of Mlp1/2 to mature NPCs prevents their localization in the nucleolar territory. Second, Nup2 leads to an increase of the residence time of all NPCs in the non-nucleolar territory possibly by mediating interactions with chromatin.

## Results

### doRITE allows the visualization of individual NPCs in living budding yeast cells

Live-cell imaging of individual fluorescently tagged NPCs in budding yeast cells is severely limited by the high NPC density in the NE (>10 NPC/$\mu m^2$) (Winey, Yarar, Giddings, & Mastronarde, 1997). To enable the visualization of individual NPCs, we reduced the density of fluorescently labelled NPCs on the nucleus by recombination-induced tag exchange (RITE) (Verzijlbergen et al., 2009). In RITE, a protein tag is genomically exchanged through Cre-induced recombination, so proteins produced before or after recombination can be distinguished by their different tags (Figure 1D). Because core Nups remain associated with individual NPCs over hours or even days (Hakhverdyan et al., 2021; Rabut, Doye, & Ellenberg, 2004), RITE can be used to distinguish between old and new NPCs (Colombi, Webster, Fröhlich, & Lusk, 2013; Onischenko et al., 2020; Toyama et al., 2019). We used a RITE-cassette that allows the switch from a GFP-labelled protein to a new protein that is not

fluorescently labelled (RITE(GFP-to-dark)) (Onischenko et al., 2020, Kralt et al., 2022). When tagging a Nup that stably associates with the NPC, we expected that successive cell divisions would dilute labelled NPCs by inheritance to both mother and daughter cells leading to a low density of labelled NPCs. By contrast, a labeled dynamic Nup is expected to redistribute to all NPCs of the nucleus and would not remain with individual NPCs (Figure 1C&D). We term this approach **d**ilution **o**f **RITE**-labelled complexes (doRITE). As a proof of concept, we performed doRITE on Nups previously reported to exhibit either stable (Nup133, Nup188) or dynamic (Nup60) association with the NPC (Hakhverdyan et al., 2021; Onischenko et al., 2020). We imaged cells at different time points after the induction of recombination (Figure 1E). For Nup133 and Nup188, foci likely from individual NPCs could be clearly distinguished after 7 hours and their intensities remained stable until only a few foci remained per cell. In contrast, the signal of Nup60 gradually decreased on all NPCs until it became undetectable over background at 11 hours (Figure 1E). Since the degradation rate of Nup60 is similar to other Nups (Hakhverdyan et al., 2021), reduction of its signal in doRITE is unlikely to be caused by protein degradation. doRITE can thus distinguish between stable and dynamically associated Nups.

To determine whether the fluorescent foci observed in doRITE at late timepoints correspond to individual NPCs, we analysed their intensity and inheritance patterns. Nup133-GFP foci exhibited a narrow intensity distribution indicative of a single particle species (Supplemental Figure S1A). The foci did not cluster at the spindle pole body, as has been described for certain compromised NPCs (Heath et al., 1995, Supplemental Figure S1B). Furthermore, 43 ± 2% (mean ± s.d.) of the foci were inherited by daughter cells (Figure 1F), which is similar to the inheritance rate previously reported for pre-exisiting NPC (38 ± 12%, Khmelinskii et al., 2010). The average number of Nup133-RITE(GFP-to-dark) and Nup188-RITE(GFP-to-dark) foci per cell decayed exponentially (Figure 1G). By fitting this decay using the experimentally determined growth rate of the cells, we estimate an average of 158 ±22 (95% confidence interval) NPCs per cell at the time of recombination induction. This is at the upper end of the range expected in yeast cells (Winey et al., 1997), but the analysis likely overestimates the true number of NPCs because labelled Nups present in the soluble pool at the time of recombination continue to be incorporated and because we consider the induction of RITE as the timepoint 0 although recombination occurs asynchronously in the cell population.

In summary, our data are consistent with the interpretation that the observed foci represent individual NPCs. We conclude that doRITE can be used (1) to analyse the association dynamics of Nups at individual NPCs *in vivo*, (2) to follow the inheritance of individual NPCs from mother to daughter cell, and (3) to obtain single-NPC resolution in live budding yeast cells with standard diffraction-limited microscopy.

## Mlp1/2 and Pml39 associate with the NPC in a stable manner

Based on FRAP experiments, it was previously reported that the nuclear basket Nups Mlp1 and Mlp2 exchange at the NPC within seconds (Niepel et al., 2013). However, a recent metabolic labelling-based biochemical analysis that systematically determined the exchange rate of all Nups on NPCs found the residence half-lives of Mlp1 and Mlp2 to be 4-5 hours (Hakhverdyan et al., 2021). To understand the function and regulation of the nuclear basket and to correctly interpret experimental results on (mis)localization phenotypes, it is crucial to know whether the basket filaments form stable or dynamic assemblies. Therefore, we performed doRITE with Mlp1 and Mlp2 to visualize their association dynamics with NPCs in living cells. For comparison, we also performed doRITE with a set of additional Nups from different NPC subcomplexes, which exhibited different dynamic behaviours by metabolic labelling (Hakhverdyan et al., 2021) (Figure 2A). In this assay, Mlp1, Mlp2 and Pml39 behaved similarly to the stable Nups of group 1 (Nup133, Nup188, Pom152, Nup82, Nup159), which have an exchange half-life of greater than 7 hours at the NPC. Individual NPCs could be clearly

distinguished starting 7 hours after induction of recombination and the intensity of individual dots remained stable through multiple cell divisions (Figure 2B, Supplemental Figure S2A). In contrast, the analysed Nups of group 3, Nup116 (linker Nup) and Gle1 (cytoplasmic export platform), exhibited gradual reduction of the GFP-signal on all NPCs similar to Nup60 and consistent with a dynamic association with the NPC (Figure 2B and Supplemental Figure S2A). Thus, Mlp1, Mlp2 and Pml39 associate stably with NPCs over multiple generations, although we cannot exclude the existence of an additional more dynamic pool of these proteins which could not be visualized by doRITE. The intensity of Mlp2-GFP and Pml39-GFP at the nuclear envelope and at individual foci was lower than that of Mlp1-GFP (Figure 2B), indicating that they are present at NPCs at a lower copy number. Quantification of the intensity of these GFP-tagged Nups on the NE in the non-nucleolar territory suggests that Mlp2 might be present in half (45.3±5 % (mean ± s.d.)) and Pml39 in one quarter (26.9±7 % (mean ± s.d.)) of the copy number of Mlp1 (Supplemental Figure S2B).

Pml39 was recently shown to anchor a subpopulation of Mlp1 to the NPC (Gunkel et al., 2023). To test whether Pml39 is required for the assembly of stable nuclear basket filaments, we performed doRITE with Nup133 and Mlp1 in *pml39Δ* cells. Similar to previous results (Gunkel et al., 2023) we observed an intensity reduction of Mlp1-GFP at the NE to 61±7% (mean ± s.d.) upon deletion of *PML39* (Supplemental Figure S2B). Mlp1-RITE(GFP-to-dark) still formed the characteristic NPC-foci after 14 hours of recombination in the absence of Pml39, but their intensity was reduced compared to wild type cells (Figure 2B, compare rows 1 and 4). This is consistent with the presence of a Pml39-dependent subpopulation of Mlp1 at the 14h-old NPCs but indicates that Pml39 is not necessary for the stability of Mlp1 binding. Deletion of *PML39* also had no effect on the dynamics of Nup133(GFP-to-dark) in doRITE (Supplemental Figure S3A).

Although Nup60 is essential for the recruitment of Mlp1/2 to the NPC, it was recently shown to be dispensable for maintenance of already assembled Mlp1/2 at the NPC in meiotic cells (King et al., 2023). We tested whether this is also the case in exponentially growing cells. Indeed, we observe that depletion of Nup60 via an auxin-inducible degron tag (Nishimura, Fukagawa, Takisawa, Kakimoto, & Kanemaki, 2009) (Supplemental Figure S2C) did not affect the localization of Mlp1-RITE(GFP-to-dark) four hours after induction of RITE, suggesting that the old Mlp1 protein pool was maintained at NPCs (Figure 2C). In contrast, when all Mlp1 was labelled (no induction of RITE), a fraction of Mlp1-GFP accumulated in a nuclear focus reminiscent of the Mlp1-GFP focus formed in *nup60Δ* cells (Feuerbach et al., 2002; Niepel et al., 2013) (Figure 2C). Since this focus is not visible when only the old protein is labelled, we conclude that it is composed of newly synthesized Mlp1 that cannot be incorporated into the NPC in the absence of Nup60. Thus, Nup60 is required for the assembly of Mlp1 into the NPC but not for its maintenance. This appears to be an evolutionary conserved mechanism, as it was also reported for the human homologues Nup153 and TPR (Aksenova et al., 2020).

## Exclusion of old NPCs from the nucleolar territory is mediated by Mlp1

Next, we wanted to better understand the exclusion of Mlp1/2-positive NPCs from the nucleolar territory. Since integration of Mlp1 and Mlp2 into the NPC occurs on average within one hour of assembly (Onischenko et al., 2020), we expected that the NPCs visualized as individual foci by doRITE at the 14-hour timepoint would all carry Mlp1/2 and thus be excluded from the nucleolar territory. Indeed, only 10±3 % (mean ± s.d.) of 14 h-old Nup133-RITE(GFP-to-dark) NPCs were detected in the nucleolar territory marked by a nucleolar protein tagged with red fluorescent protein (Nop1-RFP). These could correspond to occasional nucleolar localized Mlp1-positive NPCs (Bensidoun et al., 2022). Deletion of *MLP2* did not significantly change this distribution. However, in *mlp1Δ* and *mlp1Δ*

*mlp2Δ* cells, the fraction of 14-hour old NPCs detected in the nucleolar territory increased to 15±2 % and 19±4 %, respectively (Figure 3A), suggesting that indeed Mlp1/2 are important for the exclusion of NPCs from the nucleolar territory. Importantly, doRITE with Nup133-RITE(GFP-to-dark) showed that the deletion of the basket protein genes did not compromise the stability of the NPC core (Supplemental Figure S3A). Next, we asked whether there was a change in the overall NPC density in the nucleolar territory in *mlp1Δ mlp2Δ* cells. Overall NPC density is lower in the nucleolar territory relative to the rest of the nuclear envelope in wildtype cells (Wang et al., 2016). We quantified NPC density in wild type and mutants strains by measuring the GFP intensity of Nup133-GFP without the induction of RITE in the nucleolar and non-nucleolar section of the nuclear envelope (Figure 3B). We found that NPC density in the nucleolar territory was 53±6% of that in the non-nucleolar territory in wild type cells but increased to 75±7% in the absence of Mlp1 and Mlp2 (Figure 3B).

Since newly assembled NPCs also lack Mlp1 and Mlp2, we tested whether they exhibit a similar distribution as 14 h-old NPCs in *mlp1Δ mlp2Δ* cells. We used an inverted RITE cassette (dark-to-GFP) to visualize newly assembled NPCs (Supplemental Figure S3B). Nup133-RITE(dark-to-GFP) generated a more diffuse NE signal at early timepoints that made the identification of individual newly assembled NPCs difficult – possibly due to the interaction of Nup133 with the membrane via an amphipathic helix (Nordeen, Turman, & Schwartz, 2020). We therefore used Nup188 to compare the fraction of old (GFP-to-dark at 14 h) and new (dark-to-GFP at 45 min) NPCs in the nucleolar territory. We detected 6.1±1.0 % of 14-hour old NPCs in the nucleolar territory. In contrast, 14.2 ±1.4 % of newly assembled NPCs localized there (Figure 3C), which is comparable to the fraction of old NPCs observed in the nucleolar territory in *mlp1Δ mlp2Δ* cells. This suggests, that in the absence of Mlp1/2, 14 h-old NPCs behave similar to newly assembled NPCs with respect to their nucleolar localization. In contrast, no difference in localization to the nucleolus was observed for old and new NPCs labelled with Mlp1-RITE (Supplemental Figure S3C). Since this population of "new" NPCs has already acquired Mlp1, this is consistent with the conclusion that the presence or absence of Mlp1/2 is a major determinant in mediating nucleolar exclusion of NPCs.

Next, we tested which domain of Mlp1 mediates the exclusion from the nucleolus. A domain encompassing amino acids 338-616 of Mlp1 mediates localization to the NPC via binding to Nup60 and was reported to localize homogeneously to all NPCs (Cibulka et al., 2022; Niepel et al., 2013). We expressed truncated forms of Mlp1 tagged with GFP in *mlp1Δ* cells: the NPC binding fragment alone (ΔNΔC) or including the endogenous N- or C-terminal part of Mlp1 (Schematic representation Figure 3D). All three fragments were excluded from the nucleolar territory (Figure 3D, Supplemental Figure S3D), suggesting that the NPC-binding domain is sufficient to mediate the exclusion. Since we observed lower NE signal for Mlp1(ΔN)-GFP and Mlp1(ΔNΔC)-GFP, we expressed Mlp1(ΔNΔC)-GFP from a CEN plasmid in *mlp1Δ mlp2Δ* cells. In cells with low expression, Mlp1(ΔNΔC)-GFP was excluded from the nucleolar territory whereas in rare, highly expressing cells the construct localized homogenously to all NPCs, as previously reported (Niepel et al., 2013, Supplemental Figure S3E). This could indicate that the fragment preferentially binds NPCs in the non-nucleolar territory but can in principle also associate with NPCs the nucleolar territory.

The exclusion of Mlp1-positive NPCs from the nucleolar territory could be due to their retention in the non-nucleolar territory, e.g. via their interactions with nascent mRNA and mRNA maturation factors (Bensidoun et al., 2022; Bermejo et al., 2011; Saroufim et al., 2015). To test whether transcription affects nucleolar exclusion, we analysed Mlp1-GFP labelled NPCs in cells with an auxin-inducible degron tag on the Rpb2 subunit of Polymerase II (Pol II) (Derrer et al., 2019) (Supplemental Figure S3F). As reported in Bensidoun et al. (2022), we observed an increase in the nucleoplasmic signal of Mlp1 upon depletion of Pol II (Figure 3E). However, Mlp1-containing NPCs remained

excluded from the nucleolar territory (Figure 3E). Thus, although inhibition of transcription affects nuclear basket assembly, the exclusion of Mlp1-containing NPCs from the nucleolus is maintained.

## Nup2 restricts the localization of NPCs to the nucleolar territory independent of their age

Even in *mlp1Δ mlp2Δ* cells, the NPC density in the nucleolar territory remained reduced relative to the rest of the nuclear envelope (Figure 3B). This suggests that an additional, Mlp-independent mechanism is involved in restricting the localization of NPCs in the nucleolar territory. To test whether the nuclear basket contributes to this, we quantified the NPC density in the nucleolar and non-nucleolar territory in additional basket mutants by measuring the average fluorescent intensity of Nup133-GFP in these regions. Deletion of *NUP60* led to a largely homogenous distribution of the NPCs around the entire nucleus and the density ratio of the nucleolar vs. non-nucleolar territory was close to 1 (0.93 ±0.07) (Figure 4A+B). To test whether removal of Nup60 changes the distribution of NPCs also when Mlp1/2 are still present at the NPCs, we applied auxin-mediated depletion of Nup60 to cells expressing Nup133-RITE(GFP-to-dark) 5 hours after RITE induction. We observed an increased density of >5 hour-old NPCs in the nucleolar territory upon depletion of Nup60 (Supplemental Figure S4A+B). This suggests that a fraction of >5 hour-old NPCs is devoid of Mlp1/2 and can enter the nucleolar territory upon removal of Nup60. Mlp1-positive NPCs remained excluded from the nucleolar territory (Figure 2C, Supplemental Figure S4C). Thus, Nup60 reduces the density of NPCs in the nucleolar territory via an Mlp1/2 independent mechanism. Nup60 recruits Nup2 to the NPC (Dilworth et al., 2001) and we therefore asked, whether Nup2 was involved in nucleolar exclusion. Like *nup60Δ* cells, *nup2Δ* cells exhibited a nearly homogeneous distribution of NPCs over the entire NE (Figure 4B). Since Mlp1-positive NPCs remain excluded from the nucleolar territory in *nup2Δ* cells (Galy et al., 2004), the homogenous distribution observed in this mutant must be caused predominantly by the redistribution of Mlp-negative NPCs into the nucleolar territory. The phenotype of *nup2Δ* cells was copied in cells carrying a deletion of the 35 C-terminal amino acids of Nup60 (*nup60ΔC)* containing the binding region for Nup2 (Nup2-BR) (Cibulka et al., 2022) (Figure 4B, scheme) either in the presence or absence of Nup2. This clearly attributes the nucleolar exclusion of NPCs to the recruitment of Nup2 to the NPC.

Taken together, we conclude that two independent molecular mechanisms lead to a reduced NPC density in the nucleolar territory. First, NPCs become depleted from the nucleolar territory once they bind the nuclear basket proteins Mlp1/2. Second, Nup2 mediates the indiscriminate exclusion of additional NPCs from the nucleolar territory.

## Basket components affect the mobility of NPCs in the NE

The partial depletion of NPCs from the nucleolar territory could be caused by interactions that prolong the time spent in the non-nucleolar territory, since the nuclear basket is known to interact with multiple partners that can bind to chromatin (reviewed in Sumner & Brickner, 2022). More interactions in the non-nucleolar territory should manifest in a lower mobility of the NPCs in this region in wild type cells. In contrast, in *nup60Δ* cells, where we observe a homogeneous distribution of NPCs (Figure 4A&B), the mobility of NPCs would be expected to be the same throughout the NE. To test this idea, we applied simulations and tracking of individual NPCs using our probabilistic method, ExTrack (Simon, Tinevez, & van Teeffelen, 2023).

First, we confirmed in a 2D simulation that a local decrease in the diffusion coefficient indeed causes a local increase in particle density (Figure 5A). Next, we compared the diffusion of Nup133-RITE(GFP-to-dark)-labelled NPCs 14 h after induction of recombination in wild type cells (Movie 1, Figure 5B) and in different nuclear basket deletion mutants (*nup60Δ*, *mlp1Δ*, *mlp2Δ* and *mlp1Δ mlp2Δ)*. We

reasoned that these 14 h-old NPCs, which would be predominantly Mlp-positive in wild type cells and Mlp-negative in basket mutants, should show differences in mobility, if mobility is influenced by the presence of Mlp1/2. In wild type cells, NPC mobility exhibited behaviour switching between immobile, slow diffusive, and fast diffusive states (states 1, 2, & 3, Figure 5C&D). Interestingly, we detected changes in the fractions of NPCs that occupied the different diffusion states in different mutants (Figure 5D). NPCs in *mlp1Δ mlp2Δ* double mutants and *nup60Δ* mutants spend more time in the fast diffusive state relative to the wild type, while the diffusion coefficients of these states were similar in all analysed strains (Supplemental Figure S5A). This population shift translates into an overall increase in the average diffusion coefficients of these strains, where *mlp1Δ mlp2Δ* and *nup60Δ* had average diffusion coefficients that were 63±8 % and 53 ±14 % higher than the wild type, respectively (Figure 5E). This is consistent with previous FRAP experiments that showed increased mobility of NPCs in *mlp1Δ mlp2Δ* cells (Niepel et al., 2013; Spichal et al., 2016). To test if this change in the movement behaviour could explain the changes in NPC distribution, we modelled the diffusion of NPCs along a spherical nucleus, applying diffusion parameters from *nup60Δ* cells in a cap region representing the nucleolar territory and from wild type cells in the rest of the NE (Figure 5F, see Track Simulations in the Methods). This relatively simple simulation generates a model where at steady state, the density of NPCs in the nucleolar territory would be 76 ±3 % of that in the non-nucleolar territory (Figure 5G).

Our data and simulation thus support the hypothesis that an increased apparent diffusion coefficient of NPCs on the nuclear envelope contributes to the reduced NPC density in the nucleolar territory (Figure 5A, F&G). Indeed, the tracks from *mlp1Δ mlp2Δ* and *nup60Δ* cells exhibit a reduced frequency of binding events, that is, less transitions from a diffusive to a bound state (Supplemental Figure S5B). This would be consistent with reduced interactions of NPCs with nuclear components in these strains. However, since the two mutants exhibit similar average diffusion coefficients (Figure 5E), the observed difference in mobility can probably be attributed to the loss of Mlp1/2 only, which is absent in both mutants. This interpretation is corroborated by the observation that acute depletion of Nup60, which does not affect the localization of Mlp1, did not affect NPC mobility (Supplemental Figure S5C). Thus, we cannot at this point tease apart the Mlp1-dependent and Mlp1-independent roles of Nup60. Furthermore, the nucleolar NPC density predicted in our model is still significantly higher than what we observe experimentally (76 ±3 % in the model versus 53±6 % in wild type cells, compare Figure 5G to Figure 4B). Therefor, while our results support the hypothesis that NPC distribution can be the result of differential mobility caused by different interaction networks in the different regions of the nucleus, additional mechanisms are likely to contribute (Figure 6).

## Discussion

### doRITE as a versatile tool for single NPC analysis in yeast

To understand the differences between NPC variants, it is crucial to develop methods that do not only report on bulk behaviour but can distinguish between subpopulations of NPCs and ideally provide single NPC resolution. While single NPCs can readily be resolved by confocal microscopy on the flat bottom of many adherent mammalian cell types, this poses a greater challenge in budding yeast, which have small, spherical nuclei with high NPC density. In this work, we developed RITE into a versatile tool to achieve single NPC resolution in *S. cerevisiae* by utilizing the properties of yeast NPCs: (i) high stability of the complex, (ii) multiple copies of the labelled protein per complex, and (iii) intact inheritance through multiple cell cycles (Figure 1D&E). We harnessed the power of this method to analyse the exchange dynamics of different Nups at the NPC (Figure 2), to determine the localization of single NPCs relative to nuclear landmarks (Figures S1B, 3&4) and to track the

movement of NPCs along the NE (Figure 5). The NPC is particularly suitable for doRITE due to the presence of several copies of the labelled protein per complex which yields a high signal-to-noise ratio and enables tracking of individual NPCs, but in principle, doRITE could also be applied to other stable complexes such as the ribosome.

## The nuclear basket filaments form a stable structure on the NPC

FRAP is a common method to investigate the dynamics of biological molecules and has been used to systematically characterize Nup dynamics in mammalian cells (Rabut et al., 2004). However, only highly dynamic interactions at NPCs, like those of transport receptors, can be quantified by FRAP in budding yeast (Derrer et al., 2019), since longer measurements are confounded by the mobility of entire NPCs on the nuclear surface. doRITE overcomes this limitation and provides a complementation to biochemical assays, which were recently used to determine the exchange rate of Nups on the NPC in bulk (Hakhverdyan et al., 2021; Onischenko et al., 2020).

Our results are largely in agreement with the previously reported overall categorisation of Nups as stable or dynamic based on biochemical data (Figure 2, (Hakhverdyan et al., 2021)). However, we observed that the Nups from group 2 (Mlp1, Mlp2, Nup53 and Nup100), with reported residence times at the NPC of 4.5-5 hours, exhibit stable properties in our doRITE assay, similar to the stable core Nups of group 1 (Figure 2B). This discrepancy could arise from the presence of two pools with different dynamic behaviour, of which the mass-spectrometry approach would observe the average while our doRITE approach would primarily visualize the more stable pool. The interpretation of Mlp1 as a stable Nup is corroborated by the observation that, once assembled, it is maintained at the NPC independent of Nup60 (Figure 2C), as also reported for meiotic budding yeast and mammalian cells (Aksenova et al., 2020; King et al., 2023). Furthermore, the human homologue TPR has been shown to exhibit stable association with the NPC (Souquet et al., 2018). Interestingly, Mlp1 also forms stable assemblies at the NPC when *PML39* is deleted (Figure 2B), suggesting that the additional copies of Mlp1 recruited to the NPC by Pml39 (Gunkel et al., 2023) are not required for the assembly of stable nuclear basket filaments. Although we present clear evidence for the stable assembly of Mlp1, Mlp2 and Pml39 at the nucleoplasmic face of the NPC, we cannot exclude the possibility that a second, more mobile pool exists which might be associated with the NE more generally, as suggested by labelling at NE sites away from the NPCs by immuno-gold (Strambio-de-Castillia et al., 1999). Furthermore, transient interactions via Nup60 could prevail during early assembly stages before being converted into more stable interactions during maturation of the nuclear basket.

Quantification of the amounts of GFP-tagged basket components at the NE suggest that the relative abundance of Mlp1:Mlp2:Pml39 is 4:2:1 (Supplemental Figure S2B). The structure and stoichiometry of the majority of the core NPC is now well characterized thanks to high resolution cryo-ET data and structural modelling (e.g. Akey et al., 2022, Akey et al., 2023, Allegretti et al., 2020, Kim et al., 2018) (Akey et al., 2023, 2022; Allegretti et al., 2020; Kim et al., 2018). Recent work has also started to shed light on the structure of the nuclear basket (Singh et al., 2024), but it is as yet not of sufficient resolution to inform the abolute copy number of all nuclear basket components. Copy numbers of 16 and 8 for Mlp1 and Mlp2 respectively would be consistent with previous mass-spectrometry- or fluorescence microscopy-based quantification (Kim et al., 2018; Mi, Goryaynov, Lindquist, Rexach, & Yang, 2015). Surprisingly, this would suggest a copy number as low as four for Pml39, suggesting that it might not be present in every spoke. Since Pml39 can interlink Mlp1 molecules (Gunkel et al., 2023), we propose that Pml39 might connect the basket proteins of neighboring spokes, which would be consistent with the localization to the distal ring reported for the mammalian homologue ZC3HC1 (Gunkel et al., 2023).

ZC3HC1, anchors 50% of the TPR molecules to the NPC (Gunkel et al., 2023). As previously reported (Gunkel et al., 2023), the reduction of the NE-signal of Mlp1 upon deletion of *PML39* in yeast is less than 50% (Supplemental Figure S2B). However, these measurements are hampered by an increased background from the nucleoplasmic soluble pool in the deletion mutant, and it is therefore possible that also in yeast 50 % of the Mlp1 molecules are anchored to the NPC by Pml39. One possible explanation for this organization could be that Mlp1/Mlp2 heterodimers bind to the NPC via interaction with Nup60 and the outer ring (Akey et al., 2022; Cibulka et al., 2022; Kim et al., 2018)and an additional set of four Mlp1/Mlp1 homodimers is anchored by four copies of Pml39. However, further analysis will be needed to determine the exact stoichiometry and structural organization of the nuclear basket components.

### *NPC retention in the non-nucleolar territory of the NE is mediated by the basket proteins Mlp1/2 and Nup2*

It has previously been observed that Mlp-positive NPCs are excluded from the nucleolar territory (Galy et al., 2004; Niepel, Strambio-de-Castillia, Fasolo, Chait, & Rout, 2005). In this work, we show that this phenomenon affects predominantly old NPCs (Figure 3A-C), which is in agreement with the observation that Mlp1/2 are assembled into NPCs after a long delay. We consider two hypotheses for the molecular mechanism of exclusion: retention in the non-nucleolar region due to interaction with chromatin and/or mRNA (Figure 6, blue arrow), or a barrier that prevents entry of Mlp-positive NPCs into the nucleolus (Figure 6, red inhibition signal). Depleting RNA Pol II did not cause Mlp-positive NPCs to redistribute to the nucleolar region (Figure 3E), suggesting that exclusion does not rely on tethering to nascent mRNA or transcribing gene loci. Since even the minimal NPC binding domain of Mlp1 exhibited preference for the NPCs outside of the nucleolar territory (Figure 3D), nucleolar exclusion might also involve regulation through the Mlp1 binding site. Further studies are needed to determine exactly which molecular mechanisms are at play.

Alternatively, exclusion could be mediated by the specific biophysical properties of the nucleolus (reviewed in Tartakoff et al., 2022), which could present a barrier for entry to Mlp-positive NPCs. Since the free pool of Mlp1 in principle has access to the nucleolus (Bensidoun et al., 2022), it is possible that the barrier applies only to the NPC as a whole, or to the fully assembled basket.

In addition, we describe a second, Mlp-independent mechanism that leads to a reduced density of NPCs in the nucleolar territory and relies on Nup2 (Figure 4D). Like Mlp1, Nup2 and its homologues in *Aspergillus nidulans* and metazoa have been shown to interact with chromatin (Holzer et al., 2021; Ishii, Arib, Lin, Van Houwe, & Laemmli, 2002; Markossian, Suresh, Osmani, & Osmani, 2015), which could lead to the preferred localization of NPCs to the non-nucleolar region of the NE.

Using doRITE, we were able to track the diffusion of individual NPCs on the nuclear envelope of budding yeast up to 30 s, yet, many tracks were shorter, since NPCs diffused out of the focal plane. However, employing a probabilistic approach that considered the dynamics and populations in groups of single particle trajectories (Simon et al., 2023), we could determine the diffusion coefficients of NPCs in different mobility states from our tracking data. Our analysis overall supports the hypothesis that the modulation of diffusion due to differential interactions can lead to a non-homogeneous distribution of NPCs on the NE (Figure 5). In the future, the tracking and analysis pipeline we developed will be applicable to further study the forces that act on NPCs and drive their movement and distribution on the nucleus.

In conclusion, we have developed and applied a versatile new tool to better understand the properties and organization of the nuclear basket. We anticipate that the high signal-to-noise achievable using doRITE will prove useful in answering the many questions that remain regarding the regulation of basket assembly and its functional role in the NPC.

## Materials and Methods

### Yeast strain and plasmid construction

*Saccharomyces cerevisiae* strains were created in the BY4742 wild type strain background using standard yeast genetic techniques by transformation of either a PCR product (Longtine et al., 1998) or a linearized plasmid with homology regions to the yeast genome. Some strains with multiple genetic modifications were generated by mating, sporulation and spore selection. Plasmids were generated using standard restriction-based cloning methods. The V5 tag in the original RITE plasmid pKV015 from (Verzijlbergen et al., 2009) was replaced due to the presence of unfavourable codons that led to low expression levels of tagged proteins in yeast. Used strains, plasmids and primers are listed in Supplemental Tables 1-3.

### Yeast culture conditions and treatments

Yeast cultures were grown to saturation and diluted to OD=0.01 in synthetic complete medium containing 2% glucose at 30°C. Prior to induction of recombination, cells were kept and grown on selective (-ura or hygromycin) solid or liquid medium to select against a low level of uninduced recombination from the Cre recombinase which is continuously expressed under control of a TDH3 promoter (Terweij et al., 2013). Exponentially growing cells were induced to recombine with 0.5 µM β -estradiol (Sigma), and cultures were imaged in exponential growth phase after the indicated times, if not mentioned otherwise. Auxin-inducible degradation of proteins was induced by treatment with 0.5 mM indole-3-acetic acid (IAA) (Sigma, I2886-5G, CAS: 87-51-4) and 4 µM phytic acid dipotassium salt (Sigma, 5681, CAS: 129832-03-7) for the indicated time.

### Microscopy

Cells were imaged in 384-well plates (Matrical) coated with concanavalin A for immobilization. 3D volume stacks of yeast cells with RITE-labelled NPCs were acquired on a temperature-controlled inverted Nipkow spinning disk microscope equipped with the Yokogawa Confocal Scanner Unit CSU-W1-T2 SoRa and a triggered Piezo z-stage (Mad City Labs Nano-Drive). It was used in spinning disk mode with a pinhole diameter of 50 µm combined with a 1.45 NA, 100x objective and controlled by the NIS Elements Software (Nikon). Images were acquired with a sCMOS Hamamatsu Orca Fusion BT camera (2304 x 2304 pixel, 6.5 x 6.5 µm pixel size). Imaging was performed at 30 °C with 50 % laser intensity of a Oxxius 488 nm 200 mW LNC Version and/or 5% laser intensity of Oxxius 561 nm 200 mW LNC Version light source. Z-stack data were taken with the Piezo stage in triggering mode with 0.2 µm sectioning. Exposure times were 200 ms for GFP and 50 ms for RFP.

NPC-tracking experiments were performed on a temperature-controlled inverted Nipkow spinning disk microscope equipped with the Yokogawa Confocal Scanner Unit CSU-W1-T2 controlled by the VisiVIEW Software (Visitron). It was used in spinning disk mode with a pinhole diameter of 50 µm combined with a 1.45 NA, 100x objective. The microscope is equipped with two EMCCD Andor iXon Ultra cameras (1024x1024 pixel, 13x13um pixel size) and was used in a dual camera mode for measuring distances between NPCs and spindle pole bodies, in single camera mode for all tracking experiments. Imaging was performed at 30 °C with 80 % laser intensity of a DPSS 488 nm 200 mW and/or Diode 561 nm, 200 mW light source. Timelapse data were taken with 100 ms exposure time in stream mode for 300 frames. Z-stack data for Supplemental Figure S1B were taken with the Piezo stage in triggering mode with 0.2 µm sectioning.

### Western blotting

Logarithmically growing cells were collected and lysed with 0.1 M NaOH for 15 min. Lysate was resuspended in SDS-loading buffer and 1 OD of cells were separated in 10 % acrylamide SDS-PAGE

gels. Blotting of proteins was done with a Biorad semi-dry system in TBE buffer (pH=8.3) at 25 V and 1 Amp followed by a Ponceau-S quick protein stain. V5 epitope and Crm1 detection was performed with the following antibodies: mouse-anti-V5 antibody (AbD Serotec, MCA1360), goat-anti-mouse coupled to Alexa680 (Thermo Fisher, A-21057), rabbit-anti-Xpo1 (Zeitler & Weis, 2004) and goat-anti-rabbit coupled to IRDye800 (LI-COR Biosciences GmbH, P/N 926-32211).

## Inheritance tracking

Images were acquired on the Visitron Spinning Disk microscope (see above). Cells were imaged 14 hours after RITE induction with β-estradiol at 3 min intervals in the brightfield channel to follow individual division events and identify mother-daughter pairs. At the end of the time-lapse movie, a single 3D stack was acquired in the GFP channel, and 100 mother-daughter pairs were analysed per biological replicate.

## Intensity analysis of nucleolar versus non-nucleolar NE

The intensity was analysed in three biological replicates on at least 50 nuclei per condition and replicate. On maximum z-projections, nuclei in which the nucleolus presented a moon-shaped side view abutting the NE were selected manually for analysis. For each nucleus, the z-slice with the maximum intensity for the nucleolar channel (Nop1-RFP) was selected for the intensity measurement. A hand-drawn line of width 3 pixels following the NE as delineated by the Nup-GFP signal was created in FIJI first on the non-nucleolar side of the nucleus and then on the nucleolar side. Out-of-cell background was subtracted, and the ratio between the nucleolar and the non-nucleolar signal calculated.

## Image and Data analysis

Image analysis and adjustments were carried out in FIJI (Schindelin et al., 2012). Data analysis, curve fitting, statistical analysis and plotting was carried out in Excel, Matlab or GraphPad Prism. For line scans quantifying NE signal in doRITE (Figures 1E, 2B, S2A), 20 cells were picked on maximum projections, the central slice of the z-stack was determined, and a line drawn perpendicular to the plane of the NE through the brightest spot on the NE. The profiles were aligned at the peak intensity, averaged and normalized for each strain between background and peak intensity at the 0h timepoint.

## Single Particle Tracking

NPC trajectories were extracted from the movies using the FIJI (Schindelin et al., 2012) plugin Trackmate (Ershov et al., 2022). Briefly, peaks were identified using the LoG detector method with a radius of 300 nm and a quality threshold of 25. Tracks were then reconstructed from localizations using the option *simple LAP tracker* without gaps and a maximum linking distance of 300 nm. A mask based on thresholding and dilation was applied to exclude regions of high fluorescence intensity to avoid mislocalizations in regions with higher NPC densities. Additionally, tracks were filtered to have at least 5 time points, an average quality of at least 35, and a minimum quality of 25. To avoid tracks that might contain incorrectly linked localizations from one frame to the next, we also discarded tracks within 1 µm of one another. The resulting dataset was analysed using ExTrack, our probabilistic multi-state analysis pipeline (Simon et al., 2023). We used a 3-state model, since it fit the data much better than a 2-state model. For a data set of 57 tracks of 30 time points, the likelihood of the three-state model was $1.4 \times 10^5$ higher than for two states (Vaart, 1998). We extracted the diffusion coefficients of the three states for each replicate of every condition (Supplemental Figure S5A). Due to the similarity across many tested conditions, subsequent analysis used the rounded average values for the three states, 0.001 $\mu m^2/s$ (immobile state), 0.005 $\mu m^2/s$ (slow state), and 0.03 $\mu m^2/s$ (fast state), to compare the transition rates between states (Supplemental Figure S5B). These estimated transition rates were used to compute the population

fractions at equilibrium (Figure 5D). To calculate the average diffusion coefficients (Figure 5E), we computed the weighted average for each condition ($D_{avg} = F_1D_1 + F_2D_2 + F_3D_3$), where $F_N$ is the fraction in the Nth state and $D_N$ is the corresponding diffusion coefficient. Finally, for each individual track, we computed the probability of being in each state per timepoint (Figure 5B).

## Track simulations

To explain the differences of density between the non-nucleolar and nucleolar regions, we simulated tracks moving in an environment with two different diffusion characteristics in 2D (Figure 5A) and 3D (Figure 5F). In the 2D simulation, we characterized the impact of a change in diffusion coefficient on particle density by modelling two areas with distinct diffusion coefficients using 5000 trajectories with 5000 time steps each to find the distribution of positions at steady state. Figure 5A shows the final positions of each track. In the 3D simulations, we tested whether the observed differences in the nucleolar densities could be attributed to the differences of transition rates with the three motion states at fixed diffusion coefficients (0.001, 0.005 and 0.03 $\mu m^2/s$, Supplemental Figure S5A). Tracks were simulated on a 1 µm radius sphere composed of a body and a circular cap whose surface area was one third of the total area to represent the nucleolar region. Figure 5F shows three example tracks. In these tracks, the states switched stochastically in time according to a Markov chain model of transition probability per step of $p_{12} = 0.028$, $p_{13} = 0$, $p_{21} = 0.013$, $p_2 = 0.041$, $p_{31} = 0$, $p_{32} = 0.15$ in the cap (nucleolus) and $p_{12} = 0.055$, $p_{13} = 0$, $p_{21} = 0.035$, $p_{23} = 0.02$, $p_{31} = 0$, $p_{32} = 0.2$ in the body (non-nucleolus). These transition probabilities were chosen based on the measured values for the *nup60Δ* data representing the behaviour in the nucleolar territory, and the wild type data for the behaviour in the non-nucleolar territory. 1000 tracks of 2000 time steps were used to find the steady state, where the last position of each track was used to calculate the density.

To determine how the measured diffusion coefficients could be influenced by our 2D measurements of 3D diffusion, we repeated our 3D simulations for a single diffusion coefficient (Supplemental Figure S5D) and extracted the average diffusion coefficients as a function of axial position. Near the centre of the cell, that is where our experimental data is recorded, the 2D projection decreases the apparent diffusion coefficient by half (Supplemental Figure S5E). This indicates that our reported diffusion coefficients are likely an underestimate of the true values, but within a factor of two. Notably, the differences of density depend on the ratios between diffusion coefficients. As these ratios are conserved in the 2D projections, our measured densities in simulations are not affected by the shift of diffusion coefficients.

## Author Contributions

Conceptualization: JZ, LW and ED. Methodology: JZ, ED, FS, LW. Investigation: JZ, LI, GB, AW and ED. Formal analysis: JZ, FS, LI, LW and ED. Simulations: FS, NK and LW. Writing – Original Draft: JZ, ED. Writing – Review & Editing: all authors, Funding acquisition: LW, ED. Supervision: JZ, LW, ED.

## Acknowledgements

We thank Alwin Köhler and Fred v. Leeuwen for providing plasmids, ScopeM and Joachim Hehl for microscopy support, Evgeny Onischenko, Stephanie Heinrich as well as Karsten Weis and members of his group for sharing resources, discussion and critical comments on the manuscript. The work was supported by an ETH Zurich research grant ETH-33 19-1 to ED, and in part with funding from the Polytechnique Montréal Direction de la recherche et de l'innovation (DRI) to NK and LW, the Canada First Research Excellence Fund (TransMedTech Institute) to NK and LW and the Natural Sciences and

Engineering Research Council of Canada (NSERC Discovery grant, RGPIN-2022-05142) to LW. AW acknowledges support from the Amgen Scholar Program.

## Abbreviations

AID – auxin-inducible degron
doRITE – dilution of RITE-labelled complexes
GFP – green fluorescent protein
NE – nuclear envelope
NPC - nuclear pore complex
Nup – nucleoporin
RFP – red fluorescent protein
RITE – recombination-induced tag exchange
SEM - standard error of the mean
s.d. – standard deviation

## Figure legends

**Figure 1: Single NPCs can be visualized using doRITE**

**(A)** Overview of the subcomplexes of the NPC.

**(B)** Schematic of the organization of the nuclear basket. OR (outer ring), IR (inner ring), TR (transmembrane ring). Nup60 anchors Nup2 and Mlp1 to the NPC. Mlp1 in turn is require for binding of Mlp2 and Pml39. Additional copies of Mlp1 are anchored by Pml39.

**(C)** Behavior of a stable and a dynamic Nup. Stable Nups with a long residence half-life do not exchange with soluble subunits (blue). Dynamic Nups have a short residence half-life and readily exchange with a soluble pool and between NPCs (magenta).

**(D)** Left: Schematic of the GFP-to-dark RITE cassette. A Nup of interest is tagged with a V5 tag followed by a loxP site and eGFP. Recombination leads to excision of the eGFP, so that only protein produced prior to recombination can be visualized as eGFP-tagged. ORF: open reading frame; V5: V5-tag; loxP: loxP recombination site; eGFP: enhanced green fluorescent protein. Right: Schematic of the doRITE assay showing dilution of labelled Nups through cell divisions for a stable or dynamic Nup in yeast.

**(E)** Dilution of RITE(GFP-to-dark)-labelled Nups through multiple cell divisions. Exponentially growing cells expressing the indicated Nups endogenously tagged with the RITE cassette were imaged at different timepoints after induction of RITE. Maximum projections are shown. All images are adjusted to the same brightness and contrast values. Colour bars represent membership to dynamic group in Figure 2A (blue: stable, magenta: dynamic). Schematics on left show location of Nup within the NPC. Graphs on right show radial intensity profile through fluorescent foci on the NE (compare schematic drawing on top) after indicated times of doRITE (Solid lines show mean of 20 cells, normalized for 0 h-timepoint, shaded area represents the standard deviation).

**(F)** Inheritance frequency of RITE(GFP-to-dark)-labelled NPCs from mother (M) to daughter (D) cells after 14 h of doRITE. Number of NPCs was counted in 100 M-D pairs with 1-14 pores per pair. Bar graph shows mean of three biological replicates (mean of individual replicates are shown as blue dots), error bar represents the standard deviation. Three examples of M-D pairs are shown as maximum projections. Hmg1-mCherry marks the NE.

**(G)** Mean number of labelled NPCs per cell determined from 100 cells per biological replicate at different time points after RITE(GFP-to-dark) induction for Nup133 or Nup188 (circles). The dashed line represents a fit of all shown datapoints with an exponential decay curve applying the experimentally determined doubling time of 1.75 h.

**Figure S1: doRITE foci show the characteristics of individual NPCs**

**(A)** Recombination of exponentially growing cells expressing Nup133-RITE(GFP-to-dark) were induced for 8 or 14 h, 3D stacks were acquired and integrated intensity of individual fluorescent foci was quantified. Top: Intensity distribution of 350 isolated foci. The red line represents a 2-component Gaussian fit. Bottom: Dots represent the centre peak position of the smaller component of the Gaussian fit for replicates of NPC intensity distributions 8 or 14 hours after RITE induction. Lines represent median. Each distribution contains >200 individual foci.

**(B)** Distribution of distances of Nup133-RITE(GFP-to-dark) foci at 14 h after RITE induction from the spindle pole body (SPB) labelled by Spc42-mCherry. At least 500 SPB-NPC distances were measured per replicate. Blue dots represent fraction in individual biological replicates. Error bars represent standard error of the mean. Image shows a representative maximum projection of the analysed cells.

**Figure 2: The Nups Mlp1, Mlp2 and Pml39 are stably associated with the NPC**

**(A)** Overview of the Nups analysed. Approximate positions in the NPC are marked with stars. Colours correspond to the residence half-lives as characterized by Hakhverdyan et al., 2021.

**(B)** Dilution of RITE(GFP-to-dark)-labelled Nups through multiple cell divisions. Exponentially growing cells expressing the indicated Nups endogenously tagged with the RITE cassette were imaged at different timepoints after induction of RITE. Maximum projections are shown. All images are adjusted to the same brightness and contrast values. Arrow heads indicate foci for Pml39-RITE after 14 h. Colour bars represent membership to dynamic group in Figure 2A. Schematics on left show location of Nup within the NPC. Graphs on right show radial intensity profile through fluorescent foci on the NE (compare schematic drawing on top) after indicated times of doRITE (Solid lines show mean of 20 cells, normalized for 0 h-timepoint, shaded area represents the standard deviation).

**(C)** Cells expressing Nup60 tagged with an auxin-inducible degron (AID) in the absence or presence of the E3 ligase adaptor OsTIR1 were treated with auxin for 1 h. Arrows indicate Mlp1-GFP foci, formed by newly synthesized Mlp1-GFP which cannot incorporate into the NPC in the absence of Nup60. Maximum projections are shown. Nucleoli are labelled with Nop1-RFP (magenta).

**Figure S2: Nup dynamics determined by doRITE**

**(A** Dilution of RITE(GFP-to-dark)-labelled Nups through multiple cell divisions. Exponentially growing cells expressing the indicated Nups endogenously tagged with the RITE cassette were imaged at different timepoints after induction of RITE. Maximum projections are shown. All images are adjusted to the same brightness and contrast values. Arrow highlights cytoplasmic Nup159 granule visible only before induction of RITE. Colour bars represent membership to dynamic group in Figure 2A. Schematics on left show location of Nup within the NPC. Graphs on right show radial intensity

profile through fluorescent foci on the NE (compare schematic drawing on top) after indicated times of doRITE (Solid lines show mean of 20 cells, normalized for 0 h-timepoint, shaded area represents the standard deviation).

**(B)** The mean intensity of GFP-tagged nuclear basket proteins in the non-nucleolar NE region. Signal outside the nucleus was considered as background, but for the condition Mlp1 Δpml39 the mean signal between nucleoplasm and cytoplasm was considered as background due to higher nucleoplasmic Mlp1 signal. Background subtracted signals are normalized to Mlp1. Blue dots show mean of biological replicates of at least 41 nuclei analysed per condition and replicate. Schematic shows measured area (yellow) of the NE.

**(C)** Western blot of the depletion of Nup60, in the absence or presence of the E3 ligase adaptor OsTIR1, by an auxin inducible degron (AID) at the indicated timepoints after addition of auxin (equivalent of 1 $OD_{600}$ of cells was loaded in each lane). V5 antibody detects the Nup60-V5-AID as well as the RITE-tagged Mlp1. Crm1 was used as a loading control.

**Figure 3: Exclusion of old NPCs from the nucleolar territory depends on Mlp1**

**(A)** Percentage of Nup133-RITE(GFP-to-dark) labelled in NPCs in the nucleolar territory in wild type cells and indicated mutants 14 h after RITE induction. At least 98 cells were analysed per condition and replicate by scoring the localization of NPCs in- or outside the nucleolar territory marked by Nop1-RFP. Blue dots show means of individual biological replicates and error bars the standard deviation. Stars indicate significance in one-way ANOVA with Sidak multiple comparison correction: ** $p<0.005$, ns not significant.

**(B)** Top: Example of regions of interest (ROIs) used to quantify Nup-GFP-intensity in the nucleolar and non-nucleolar region of the NE. Bottom: Mean ratio of Nup133-RITE(GFP-to-dark) in the nucleolar versus non-nucleolar territory without induction of recombination for wild type and nuclear basket deletion mutants. Blue dots show mean of biological replicates and error bars the standard deviation. At least 50 cells were analysed per replicate and condition. Stars indicate significance in one-way ANOVA with Sidak multiple comparison correction: ** $p<0.005$, ns not significant.

**(C)** Percentage of GFP labelled NPCs in the nucleolar territory for Nup188-RITE(GFP-to-dark) (old) 14 h after induction of RITE and Nup188-RITE(dark-to-GFP) (new) 45 min after induction of RITE. Image panels show maximum projections. Arrowheads point to new NPCs in the nucleolar territory. At least 70 cells were analysed per strain and biological replicate by scoring the localization of NPCs in- or outside the nucleolar territory marked by Nop1-RFP. Blue dots show means of individual biological replicates and error bars the standard deviation. Stars indicate significance in unpaired t-test: ** $p<0.005$

**(D)** Mlp1 truncations (top) and their localization upon expression in cells (bottom). The truncations were introduced into a *mlp1Δ* background. All truncations are depleted from the nucleolar territory (arrows). Due to low expression of the constructs lacking the N-terminus, the right panels are adjusted with different brightness and contrast settings (Different B/C). The nucleolus is marked with Nop1-RFP. Maximum projections are shown.

**(E)** Mlp1-positive NPCs remain excluded from the nucleolus upon depletion of PolII. RNA Polymerase II subunit Rbp2 was depleted from cells expressing Mlp1-GFP and Nop1-RFP via the auxin inducible degron. Depleted cells are larger and show increased nucleoplasmic signal of Mlp1-GFP. Arrows mark nucleoli with clear exclusion of Mlp1-GFP signal. Maximum projections are shown.

**Figure S3: Mlp1 truncations localize preferentially to non-nucleolar NPCs.**

**(A)** Exponentially growing cells expressing the indicated Nups endogenously tagged with the RITE cassette were imaged at different timepoints after induction of RITE. Maximum projections are shown. All images are adjusted to the same brightness and contrast values.

**(B)** Top: Schematic of the dark-to-GFP RITE cassette and the appearance of fluorescent Nups over time after recombination. A Nup of interest is tagged with a V5 tag followed by loxP sites flanking the selection marker. An eGFP-ORF comes into frame after recombination, so that only protein produced after recombination can be visualized as eGFP-tagged. ORF: open reading frame; V5: V5-tag; loxP: loxP recombination site; eGFP: enhanced green fluorescent protein. Bottom: Exponentially growing cells expressing the indicated Nups endogenously tagged with the RITE cassette were imaged at different timepoints after induction of RITE. Maximum projections are shown. All images are adjusted to the same brightness and contrast values.

**(C)** Percentage of GFP labelled NPCs in the nucleolar territory for Mlp1-RITE(GFP-to-dark) (old) 14 h after induction of RITE and Mlp1-RITE(dark-to-GFP) (new) 45 min after induction of RITE. At least 70 cells were analysed by scoring the localization of NPCs in- or outside the nucleolar territory marked by Nop1-RFP. Blue dots show means of individual biological replicates and error bars the standard deviation. ns: not significant by unpaired t-test.

**(D)** Mean ratio of Mlp1-truncations tagged with GFP in the nucleolar versus non-nucleolar territory. Quantification of data shown in Figure 3D. Blue dots show mean of biological replicates and error bars the standard deviation. At least 50 cells were analysed per replicate and condition. Stars indicate significance in one-way ANOVA with Sidak multiple comparison correction: * $p<0.05$.

**(E)** Localization of Mlp1ΔNΔC-GFP fragment expressed from a CEN plasmid in the absence of endogenous Mlp1 and Mlp2. Panel shows 2 nuclei with the nucleolus marked by Nop1-RFP. While most cells exhibit low expression and nucleolar exclusion of the fragment (bottom), some cells display high expression and a more homogenous NE staining (top, <5 %).

**(F)** Western blot showing the depletion of Rpb2 by an auxin inducible degron (AID) in the presence or absence of the E3 ligase OsTIR at the indicated timepoints after addition of auxin. Equivalent of 1 $OD_{600}$ of cells loaded per lane. Crm1 was used as a loading control.

**Figure 4: Exclusion of newly assembled NPCs from the nu  cleolar territory is mediated by Nup2**

**(A)** Representative nuclei of exponentially growing wild type and *nup60Δ* cells expressing Nup133-RITE(GFP-to-dark) and Nop1-RFP. Cells were imaged without induction of recombination. Single plane images are shown.

**(B)** Top: Scheme of Nup60 showing binding regions for Mlp1 (Mlp1-BR) and Nup2 (Nup2-BR). Numbers represent amino acid positions (drawn to scale). Bottom: Mean ratio of Nup133-RITE(GFP-to-dark) in the nucleolar versus non-nucleolar territory without induction of recombination for the indicated mutants. Blue dots show mean of biological replicates and error bars the standard error of mean. At least 50 cells were analysed per replicate and condition. Stars indicate significance in one-way ANOVA with Sidak multiple comparison correction: **** $p<0.0001$, ns not significant.

**Figure S4: NPC density in the nucleolar territory increases upon depletion of Nup60**

**(A)** Mean ratio of Nup133-RITE(GFP-to-dark) induction in the nucleolar versus non-nucleolar territory upon depletion of Nup60 via the auxin inducible degron. RITE was induced for four hours. Blue dots show the average of biological replicates and error bars show the standard error of the mean. At least 50 cells were analysed per replicate and condition. Star indicates significance in one-way ANOVA with Sidak multiple comparison correction: **** $p<0.0001$.

**(B)** Western blot of the depletion of Nup60 by an auxin inducible degron (AID) in the presence or absence of the E3 ligase OsTIR. V5 antibody detects both the Nup60-AID as well as the RITE-tagged Nup133. Spontaneous recombination of the RITE tag is visible by the presence of a lower molecular size of Nup133-V5 signal as cells were not grown under selection for the RITE cassette. Crm1 was used as a loading control. Equivalent of 1 $OD_{600}$ of cells was loaded in each lane

**(C)** Mean ratio of Mlp1-GFP in the nucleolar versus non-nucleolar territory upon auxin-mediated depletion of Nup60. Blue dots show mean of biological replicates and error bars the standard error of the mean. At least 50 cells were analysed per replicate and condition. No significant change was determined by pairwise t-tests (ns).

**Figure 5: The nuclear basket proteins influence the mobility of NPCs.**

**(A)** 2D simulation of 1000 particles diffusing for 2000 timesteps in two territories with different diffusion coefficients as indicated (positions in the final time point are shown). The bar graph in the bottom shows the densities of the particles found in each area at the end of the simulation.

**(B)** Still from Movie 1 showing four NPC-foci detected by Trackmate (magenta circles) with the corresponding track superimposed in red.

**(C)** Example NPC trajectories from wild type cells. The ternary colour plot shows the probability of being in a specific state at each time-point.

**(D)** Fraction of particles in different diffusion states for strains carrying deletions for different nuclear basket components. Tracks of NPCs labelled with Nup133-RITE(GFP-to-dark) obtained 14 hours after RITE induction were analysed by ExTrack with a 3-state model (immobile, slow diffusive and fast diffusive) with fixed diffusion coefficients as indicated. Bar graphs display the fraction of particles in each state computed from the transition rates between states. Results from individual biological replicates are shown as blue dots, the error bars represent the standard deviation of the three replicates. Stars indicate significance in pairwise t-tests comparing each mutant to the wild type: * $p<0.05$, ** $p<0.01$, ns not significant. At least 1100 tracks were analysed per condition and replicate.

**(E)** Average diffusion coefficients derived from data displayed in **(D)** by weighting the three diffusion coefficients according to their respective fractions. The error bars represent the standard deviation. Stars indicate significance in pairwise t-tests comparing each mutant to the wild type: * $p<0.05$, ns not significant.

**(F)** Simulation of particles diffusing on a sphere with three movement states. In the grey area, which represents the non-nucleolar territory, particles transition between states according to the rates extracted from tracking data in the wild type cells, while transition rates in the pink area, which represent the nucleolar territory, correspond to the ones from *nup60Δ* cells (Figure S5B). Three example tracks are shown and coloured according to the state the particle occupies in each timestep.

**(G)** Steady state particle density in the nucleolar region relative to the density in the non-nucleolar regions obtained from the simulation model shown in **(F)**. Data is based on 1000 tracks with 2000 timesteps each and normalized to the density in the non-nucleolar territory.

**Figure S5: Single Particle tracking of NPCs in nuclear basket mutants.**

**(A)** A 3-state model was fit to tracks obtained from labelled NPCs in exponentially growing cells expressing Nup133-RITE(GFP-to-dark) 14 hours after induction. Bar graphs show the obtained localization errors and diffusion coefficients estimated for the different mutants. The localization errors and diffusion coefficients did not differ significantly between the different strains. Results from individual biological replicates are shown as blue dots, the error bars represent the standard deviation of three biological replicates. At least 1100 tracks were analysed per condition and replicate. P value is from pairwise t-test.

**(B)** A 3-state model with fixed diffusion coefficients ($D_1$ = 0.001 µm$^2$/s, $D_2$ = 0.005 µm$^2$/s, $D_3$ = 0.03 µm$^2$/s) was fit to the same data as in (B). Transition rates between the different states are shown. Error bars represent the standard deviation. P-values are from pairwise t-tests. All other pair-wise comparisons were not significant. Transition rates shown here were used to compute fractions in different states shown in Figure 5D.

**(C)** A 3-state model with fixed diffusion coefficients ($D_1$ = 0.001 µm$^2$/s, $D_2$ = 0.005 µm$^2$/s, $D_3$ = 0.03 µm$^2$/s) was fit to tracks obtained from Nup133-RITE(GFP-to-dark) labelled NPCs expressing Nup60 tagged with an auxin-inducible degron 14 hours after RITE induction. Nup60 degradation was induced with auxin for 90 min. Degradation occurred in strains carrying the OsTIR1-E3 ligase. Bar graphs display the fraction of particles in each diffusive state. Results from individual biological replicates are shown as blue dots, the error bars represent the standard deviation. By pairwise t-test, results did not differ between conditions with or without Nup60. At least 1500 tracks were analysed per condition and replicate.

**(D)** Illustration demonstrating the projection of 3D tracks onto a 2D plane. The axes are in µm and the sphere diameter is 2 µm.

**(E)** Quantification of the measured diffusion coefficients from 3D and from projected 2D trajectories. We simulated 200,000 tracks with 11 timesteps moving on a sphere with a diffusion coefficient of 0.01 µm$^2$/s. The apparent diffusion coefficient of each track was computed by fitting a first-order polynomial to its mean squared displacements (MSD). Then, tracks were binned according to their mean z position and the average apparent diffusion coefficients were computed for each bin.

**Figure 6:** Model of how nuclear basket proteins regulate the distribution and movement of NPCs on the nucleus. Interactions with the nuclear interior (blue arrows) and lateral diffusion along the nuclear envelope (green arrows) govern the distribution of NPCs on the nuclear surface. Mlp1/2 and Nup2 independently contribute to reduced NPC density in the nucleolar territory.

**Movie 1: Tracking of individual yeast NPCs.** Nup133-RITE(GFP-to-dark) labelled cells 14 hours after induction of doRITE. Time interval 100 ms. Magenta circles indicate particle detections by Trackmate, red lines show tracks.

## References


Akey, C. W., Echeverria, I., Ouch, C., Nudelman, I., Shi, Y., Wang, J., … Rout, M. P. (2023). Implications of a multiscale structure of the yeast nuclear pore complex. *Molecular Cell*, *83*(18), 3283-3302.e5. https://doi.org/10.1016/J.MOLCEL.2023.08.025

Akey, C. W., Singh, D., Ouch, C., Echeverria, I., Nudelman, I., Varberg, J. M., … Rout, M. P. (2022). Comprehensive structure and functional adaptations of the yeast nuclear pore complex. *Cell*, *185*(2), 361-378.e25. https://doi.org/10.1016/J.CELL.2021.12.015

Aksenova, V., Smith, A., Lee, H., Bhat, P., Esnault, C., Chen, S., … Dasso, M. (2020). Nucleoporin TPR is an integral component of the TREX-2 mRNA export pathway. *Nature Communications*, *11*(1). https://doi.org/10.1038/S41467-020-18266-2

Allegretti, M., Zimmerli, C. E., Rantos, V., Wilfling, F., Ronchi, P., Fung, H. K. H., … Beck, M. (2020). In-cell architecture of the nuclear pore and snapshots of its turnover. *Nature 2020 586:7831*, *586*(7831), 796–800. https://doi.org/10.1038/s41586-020-2670-5

Bensidoun, P., Reiter, T., Montpetit, B., Zenklusen, D., & Oeffinger, M. (2022). Nuclear mRNA metabolism drives selective basket assembly on a subset of nuclear pore complexes in budding yeast. *Molecular Cell*, *82*(20), 3856-3871.e6. https://doi.org/10.1016/J.MOLCEL.2022.09.019

Bermejo, R., Capra, T., Jossen, R., Colosio, A., Frattini, C., Carotenuto, W., … Foiani, M. (2011). The Replication Checkpoint Protects Fork Stability by Releasing Transcribed Genes from Nuclear Pores. *Cell*, *146*(2), 233. https://doi.org/10.1016/J.CELL.2011.06.033

Cibulka, J., Bisaccia, F., Radisavljević, K., Carrillo, R. M. G., & Köhler, A. (2022). Assembly principle of a membrane-anchored nuclear pore basket scaffold. *Science Advances*, *8*(6). https://doi.org/10.1126/SCIADV.ABL6863

Colombi, P., Webster, B. M., Fröhlich, F., & Lusk, C. P. (2013). The transmission of nuclear pore complexes to daughter cells requires a cytoplasmic pool of Nsp1. *The Journal of Cell Biology*, *203*(2), 215–232. https://doi.org/10.1083/jcb.201305115

Derrer, C. P., Mancini, R., Vallotton, P., Huet, S., Weis, K., & Dultz, E. (2019). The RNA export factor Mex67 functions as a mobile nucleoporin. https://doi.org/10.1083/jcb.201909028

Dilworth, D. J., Suprapto, A., Padovan, J. C., Chait, B. T., Wozniak, R. W., Rout, M. P., & Aitchison, J. D. (2001). Nup2p Dynamically Associates with the Distal Regions of the Yeast Nuclear Pore Complex. *The Journal of Cell Biology*, *153*(7), 1465–1478. https://doi.org/10.1083/jcb.153.7.1465

Dultz, E., Wojtynek, M., Medalia, O., & Onischenko, E. (2022). The Nuclear Pore Complex: Birth, Life, and Death of a Cellular Behemoth. *Cells*, *11*(9). https://doi.org/10.3390/CELLS11091456

Ershov, D., Phan, M. S., Pylvänäinen, J. W., Rigaud, S. U., Le Blanc, L., Charles-Orszag, A., … Tinevez, J. Y. (2022). TrackMate 7: integrating state-of-the-art segmentation algorithms into tracking pipelines. *Nature Methods 2022 19:7*, *19*(7), 829–832. https://doi.org/10.1038/s41592-022-01507-1

Feuerbach, F., Galy, V., Trelles-Sticken, E., Fromont-Racine, M., Jacquier, A., Gilson, E., … Nehrbass, U. (2002). Nuclear architecture and spatial positioning help establish transcriptional states of telomeres in yeast. *Nature Cell Biology*, *4*(3), 214–221. https://doi.org/10.1038/NCB756

Galy, V., Gadal, O., Fromont-Racine, M., Romano, A., Jacquier, A., & Nehrbass, U. (2004). Nuclear Retention of Unspliced mRNAs in Yeast Is Mediated by Perinuclear Mlp1. *Cell*, *116*(1), 63–73. https://doi.org/10.1016/S0092-8674(03)01026-2

García-Benítez, F., Gaillard, H., & Aguilera, A. (2017). Physical proximity of chromatin to nuclear pores prevents harmful R loop accumulation contributing to maintain genome stability. *Proceedings of the National Academy of Sciences of the United States of America*, *114*(41), 10942–10947. https://doi.org/10.1073/PNAS.1707845114/SUPPL_FILE/PNAS.201707845SI.PDF

Gomar-Alba, M., Pozharskaia, V., Cichocki, B., Schaal, C., Kumar, A., Jacquel, B., … Mendoza, M. (2022). Nuclear pore complex acetylation regulates mRNA export and cell cycle commitment in budding yeast. *The EMBO*

*Journal*, *41*(15). https://doi.org/10.15252/EMBJ.2021110271

Gunkel, P., Iino, H., Krull, S., & Cordes, V. C. (2023). An evolutionarily conserved bimodular domain anchors ZC3HC1 and its yeast homolog Pml39p to the nuclear basket. *Https://Doi.Org/10.1091/Mbc.E22-09-0402*. https://doi.org/10.1091/MBC.E22-09-0402

Hakhverdyan, Z., Molloy, K. R., Keegan, S., Herricks, T., Lepore, D. M., Munson, M., … Rout, M. P. (2021). Dissecting the Structural Dynamics of the Nuclear Pore Complex. *Molecular Cell*, *81*(1), 153. https://doi.org/10.1016/J.MOLCEL.2020.11.032

Heath, C. V., Copeland, C. S., Amberg, D. C., Del Priore, V., Snyder, M., & Cole, C. N. (1995). Nuclear pore complex clustering and nuclear accumulation of poly(A)+ RNA associated with mutation of the Saccharomyces cerevisiae RAT2/NUP120 gene. *The Journal of Cell Biology*, *131*(6 Pt 2), 1677–1697. https://doi.org/10.1083/JCB.131.6.1677

Holzer, G., Magistris, P. De, Gramminger, C., Sachdev, R., Magalska, A., Schooley, A., … Antonin, W. (2021). The nucleoporin Nup50 activates the Ran guanine nucleotide exchange factor RCC1 to promote NPC assembly at the end of mitosis. *The EMBO Journal*, *40*(23). https://doi.org/10.15252/EMBJ.2021108788

Ishii, K., Arib, G., Lin, C., Van Houwe, G., & Laemmli, U. K. (2002). Chromatin boundaries in budding yeast: The nuclear pore connection. *Cell*, *109*(5), 551–562. https://doi.org/10.1016/S0092-8674(02)00756-0

Khmelinskii, A., Keller, P. J., Lorenz, H., Schiebel, E., & Knop, M. (2010, July 23). Segregation of yeast nuclear pores. *Nature*. Nature Publishing Group. https://doi.org/10.1038/nature09255

Kim, S. J., Fernandez-Martinez, J., Nudelman, I., Shi, Y., Zhang, W., Raveh, B., … Rout, M. P. (2018). Integrative structure and functional anatomy of a nuclear pore complex. *Nature*, *555*(7697), 475–482. https://doi.org/10.1038/nature26003

King, G. A., Wettstein, R., Varberg, J. M., Chetlapalli, K., Walsh, M. E., Gillet, L. C. J., … Ünal, E. (2023). Meiotic nuclear pore complex remodeling provides key insights into nuclear basket organization. *The Journal of Cell Biology*, *222*(2). https://doi.org/10.1083/JCB.202204039

Kumar, S., Neal, M. L., Li, S., Navare, A. T., Van Eeuwen, T., Wozniak, R. W., … Aitchison, J. D. (2023). Nuclear pore complexes mediate subtelomeric gene silencing by regulating PCNA levels on chromatin. *The Journal of Cell Biology*, *222*(9). https://doi.org/10.1083/JCB.202207060/214189

Longtine, M. S., Mckenzie III, A., Demarini, D. J., Shah, N. G., Wach, A., Brachat, A., … Pringle, J. R. (1998). Additional modules for versatile and economical PCR-based gene deletion and modification in Saccharomyces cerevisiae. *Yeast*, *14*(10), 953–961. https://doi.org/10.1002/(sici)1097-0061(199807)14:10<953::aid-yea293>3.3.co;2-l

Markossian, S., Suresh, S., Osmani, A. H., & Osmani, S. A. (2015). Nup2 requires a highly divergent partner, NupA, to fulfill functions at nuclear pore complexes and the mitotic chromatin region. *Molecular Biology of the Cell*, *26*(4), 605. https://doi.org/10.1091/MBC.E14-09-1359

Meinema, A. C., Marzelliusardottir, A., Mirkovic, M., Aspert, T., Lee, S. S., Charvin, G., & Barral, Y. (2022). DNA circles promote yeast ageing in part through stimulating the reorganization of nuclear pore complexes. *ELife*, *11*. https://doi.org/10.7554/ELIFE.71196

Mi, L., Goryaynov, A., Lindquist, A., Rexach, M., & Yang, W. (2015). Quantifying Nucleoporin Stoichiometry Inside Single Nuclear Pore Complexes In vivo. *Scientific Reports 2015 5:1*, *5*(1), 1–8. https://doi.org/10.1038/srep09372

Niepel, M., Molloy, K. R., Williams, R., Farrc, J. C., Meinema, A. C., Vecchietti, N., … Strambio-De-Castillia, C. (2013). The nuclear basket proteins Mlp1p and Mlp2p are part of a dynamic interactome including Esc1p and the proteasome. *Molecular Biology of the Cell*, *24*(24), 3920. https://doi.org/10.1091/MBC.E13-07-0412

Niepel, M., Strambio-de-Castillia, C., Fasolo, J., Chait, B. T., & Rout, M. P. (2005). The nuclear pore complex-associated protein, Mlp2p, binds to the yeast spindle pole body and promotes its efficient assembly. *The Journal of Cell Biology*, *170*(2), 225–235. https://doi.org/10.1083/JCB.200504140

Nishimura, K., Fukagawa, T., Takisawa, H., Kakimoto, T., & Kanemaki, M. (2009). An auxin-based degron system for the rapid depletion of proteins in nonplant cells. *Nature Methods*, *6*(12), 917–922. https://doi.org/10.1038/NMETH.1401

Nordeen, S. A., Turman, D. L., & Schwartz, T. U. (2020). Yeast Nup84-Nup133 complex structure details flexibility and reveals conservation of the membrane anchoring ALPS motif. *Nature Communications*, *11*(1), 1–12. https://doi.org/10.1038/s41467-020-19885-5

Onischenko, E., Noor, E., Fischer, J. S., Gillet, L., Wojtynek, M., Vallotton, P., & Weis, K. (2020). Maturation Kinetics of a Multiprotein Complex Revealed by Metabolic Labeling. *Cell*, *183*(7), 1785-1800.e26. https://doi.org/10.1016/J.CELL.2020.11.001

Palancade, Benoit, Liu, X., Garcia-Rubio, M., Aguilera, A., Zhao, X., & Doye, V. (2007). Nucleoporins prevent DNA damage accumulation by modulating Ulp1-dependent sumoylation processes. *Molecular Biology of the Cell*, *18*(8), 2912–2923. https://doi.org/10.1091/MBC.E07-02-0123

Palancade, Benoît, Zuccolo, M., Loeillet, S., Nicolas, A., & Doye, V. (2005). Pml39, a novel protein of the nuclear periphery required for nuclear retention of improper messenger ribonucleoparticles. *Molecular Biology of the Cell*, *16*(11), 5258–5268. https://doi.org/10.1091/MBC.E05-06-0527

Petrovic, S., Mobbs, G. W., Bley, C. J., Nie, S., Patke, A., & Hoelz, A. (2022). Structure and Function of the Nuclear Pore Complex. *Cold Spring Harbor Perspectives in Biology*, *14*(12). https://doi.org/10.1101/CSHPERSPECT.A041264

Rabut, G., Doye, V., & Ellenberg, J. (2004). Mapping the dynamic organization of the nuclear pore complex inside single living cells. *Nature Cell Biology*, *6*(11), 1114–1121. https://doi.org/10.1038/ncb1184

Saroufim, M. A., Bensidoun, P., Raymond, P., Rahman, S., Krause, M. R., Oeffinger, M., & Zenklusen, D. (2015). The nuclear basket mediates perinuclear mRNA scanning in budding yeast. *The Journal of Cell Biology*, *211*(6), 1131–1140. https://doi.org/10.1083/JCB.201503070

Schindelin, J., Arganda-Carreras, I., Frise, E., Kaynig, V., Longair, M., Pietzsch, T., … Cardona, A. (2012, July). Fiji: An open-source platform for biological-image analysis. *Nature Methods*. https://doi.org/10.1038/nmeth.2019

Simon, F., Tinevez, J. Y., & van Teeffelen, S. (2023). ExTrack characterizes transition kinetics and diffusion in noisy single-particle tracks. *The Journal of Cell Biology*, *222*(5). https://doi.org/10.1083/JCB.202208059

Singh, D., Soni, N., Hutchings, J., Echeverria, I., Shaikh, F., Duquette, M., … Villa, E. (2024). The Molecular Architecture of the Nuclear Basket. *BioRxiv*. https://doi.org/10.1101/2024.03.27.587068

Souquet, B., Freed, E., Berto, A., Andric, V., Audugé, N., Reina-San-Martin, B., … Doye, V. (2018). Nup133 Is Required for Proper Nuclear Pore Basket Assembly and Dynamics in Embryonic Stem Cells. *Cell Reports*, *23*(8), 2443–2454. https://doi.org/10.1016/J.CELREP.2018.04.070

Spichal, M., Brion, A., Herbert, S., Cournac, A., Marbouty, M., Zimmer, C., … Fabre, E. (2016). Evidence for a dual role of actin in regulating chromosome organization and dynamics in yeast. *Journal of Cell Science*, *129*(4), 681–692. https://doi.org/10.1242/jcs.175745

Strambio-de-Castillia, C., Blobel, G., & Rout, M. P. (1999). Proteins connecting the nuclear pore complex with the nuclear interior. *The Journal of Cell Biology*, *144*(5), 839–855. https://doi.org/10.1083/JCB.144.5.839

Sumner, M. C., & Brickner, J. (2022). The Nuclear Pore Complex as a Transcription Regulator. *Cold Spring Harbor Perspectives in Biology*, *14*(1). https://doi.org/10.1101/CSHPERSPECT.A039438

Tartakoff, A., DiMario, P., Hurt, E., McStay, B., Panse, V. G., & Tollervey, D. (2022). The dual nature of the nucleolus. *Genes & Development*, *36*(13–14), 765. https://doi.org/10.1101/GAD.349748.122

Terweij, M., Welsem, T. van, Deventer, S. Van, Verzijlbergen, K. F., Menendez-Benito, V., Ontoso, D., … Leeuwen, F. van. (2013). Recombination-induced tag exchange (RITE) cassette series to monitor protein dynamics in saccharomyces cerevisiae. *G3: Genes, Genomes, Genetics*, *3*(8), 1261–1272. https://doi.org/10.1534/G3.113.006213/-/DC1/006213SI.PDF

Toyama, B. H., Drigo, R. A., Lev-Ram, V., Ramachandra, R., Deerinck, T. J., Lechene, C., … Hetzer, M. W. (2019). Visualization of long-lived proteins reveals age mosaicism within nuclei of postmitotic cells. *Journal of Cell Biology*, *218*(2), 433–444. https://doi.org/10.1083/jcb.201809123

Vaart, A. W. van der. (1998). Asymptotic Statistics. *Asymptotic Statistics*. https://doi.org/10.1017/CBO9780511802256

Verzijlbergen, K. F., Menendez-Benito, V., van Welsem, T., van Deventer, S. J., Lindstrom, D. L., Ovaa, H., … van Leeuwen, F. (2009). Recombination-induced tag exchange to track old and new proteins. *Proceedings of the National Academy of Sciences*, *107*(1), 64–68. https://doi.org/10.1073/pnas.0911164107

Wang, R., Kamgoue, A., Normand, C., Léger-Silvestre, I., Mangeat, T., & Gadal, O. (2016). High resolution microscopy reveals the nuclear shape of budding yeast during cell cycle and in various biological states. *Journal of Cell Science*, *129*(24), 4480. https://doi.org/10.1242/JCS.188250

Winey, M., Yarar, D., Giddings, T. H., & Mastronarde, D. N. (1997). Nuclear pore complex number and distribution throughout the Saccharomyces cerevisiae cell cycle by three-dimensional reconstruction from electron micrographs of nuclear envelopes. *Molecular Biology of the Cell*, *8*(11), 2119–2132. https://doi.org/10.1091/MBC.8.11.2119

Zeitler, B., & Weis, K. (2004). The FG-repeat asymmetry of the nuclear pore complex is dispensable for bulk nucleocytoplasmic transport in vivo. *The Journal of Cell Biology*, *167*(4), 583–590. https://doi.org/10.1083/JCB.200407156

Fig. 1

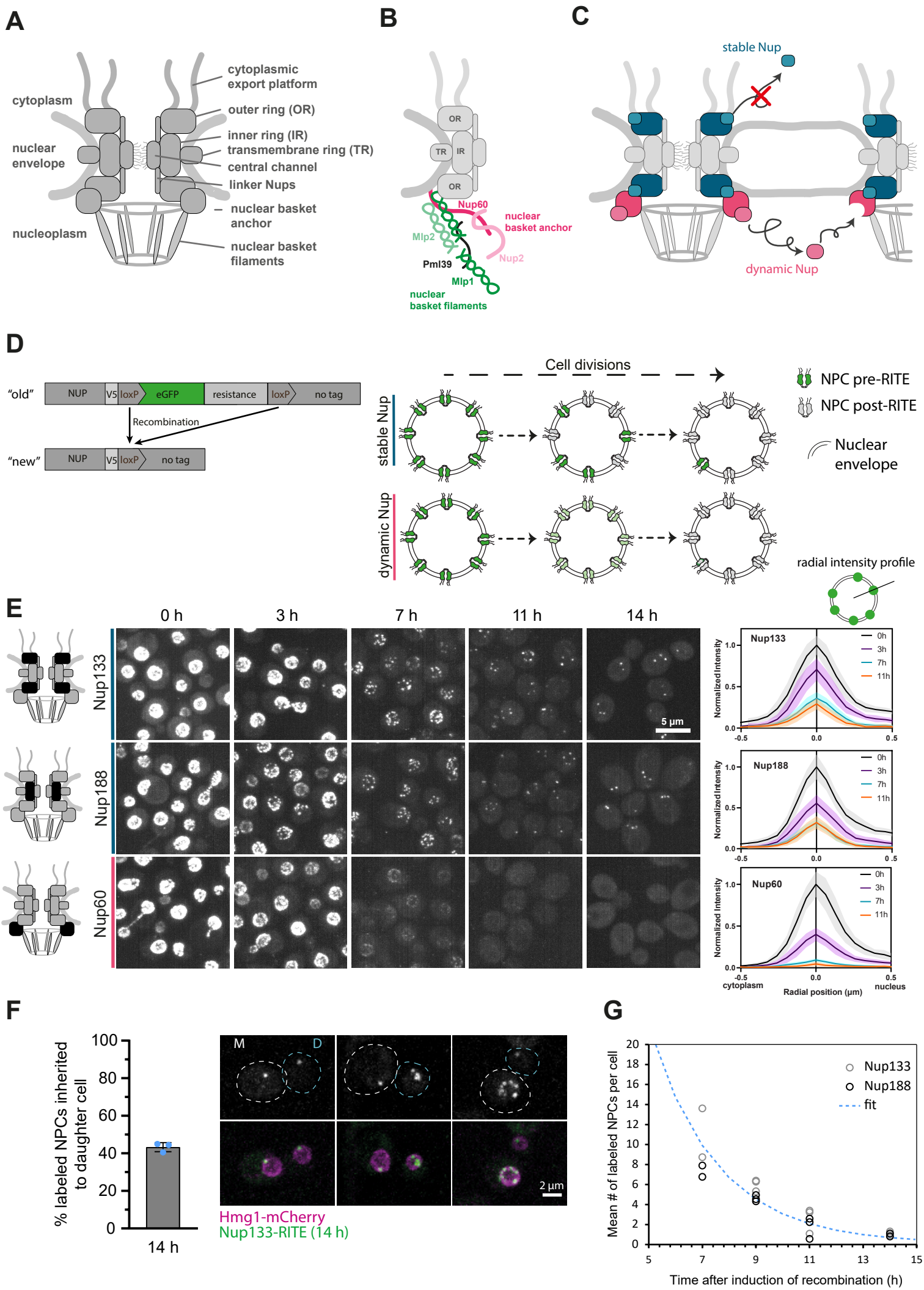
A
cytoplasm
nuclear envelope
nucleoplasm
cytoplasmic export platform
outer ring (OR)
inner ring (IR)
transmembrane ring (TR)
central channel
linker Nups
nuclear basket anchor
nuclear basket filaments
B
OR
TR
IR
OR
Nup60
nuclear basket anchor
Mlp2
Nup2
Pml39
Mlp1
nuclear basket filaments
C
stable Nup
dynamic Nup
D
"old"
NUP
V5
loxP
eGFP
resistance
loxP
no tag
Recombination
"new"
NUP
V5
loxP
no tag
Cell divisions
stable Nup
dynamic Nup
NPC pre-RITE
NPC post-RITE
Nuclear envelope
radial intensity profile
E
0 h
3 h
7 h
11 h
14 h
Nup133
Nup188
Nup60
5 µm
Nup133
Nup188
Nup60
0h
3h
7h
11h
Normalized Intensity
cytoplasm
nucleus
Radial position (µm)
F
% labeled NPCs inherited to daughter cell
14 h
M
D
2 µm
Hmg1-mCherry
Nup133-RITE (14 h)
G
Mean # of labeled NPCs per cell
Nup133
Nup188
fit
Time after induction of recombination (h)

Fig. S1:

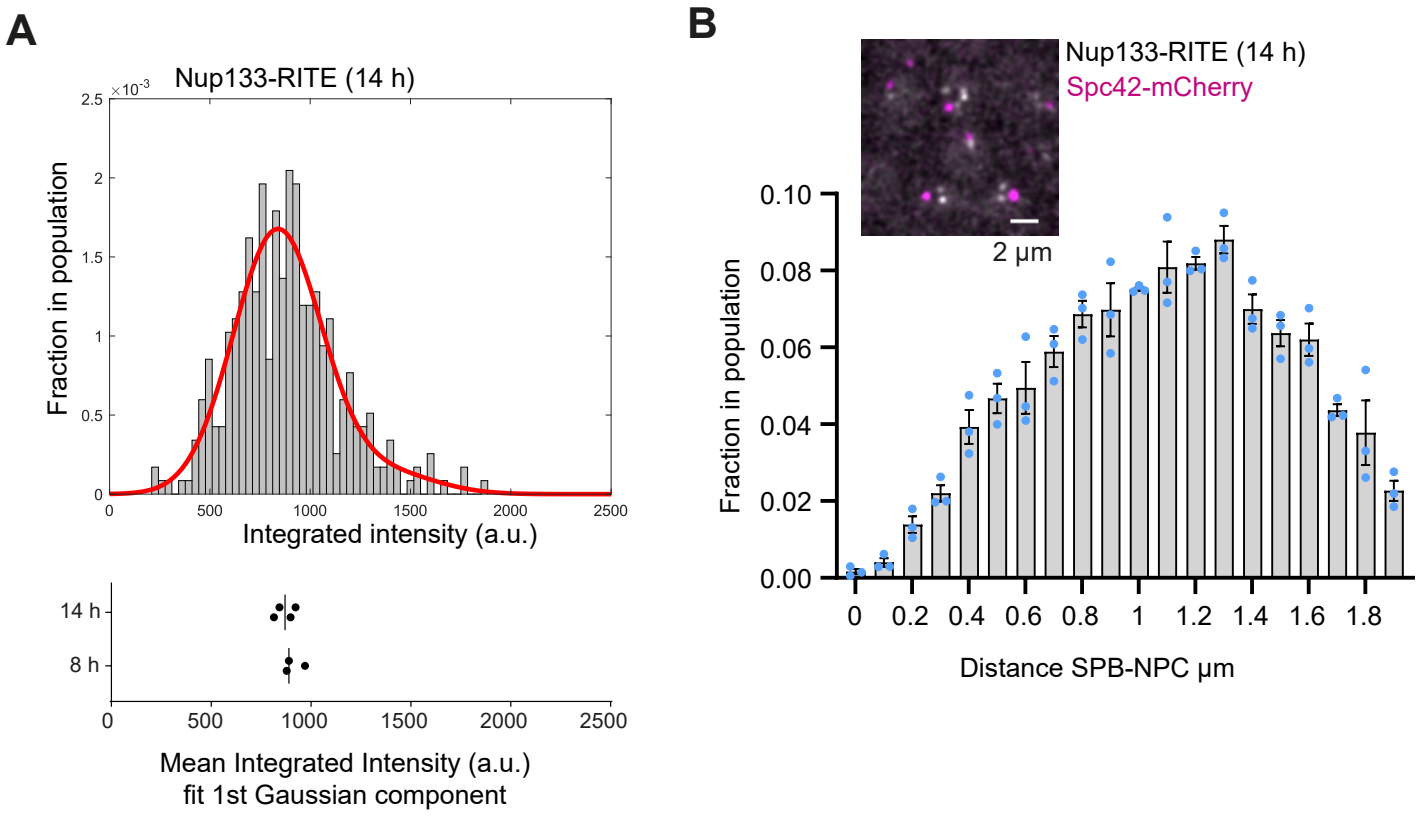
A
Nup133-RITE (14 h)
×10^-3
Fraction in population
Integrated intensity (a.u.)
14 h
8 h
Mean Integrated Intensity (a.u.)
fit 1st Gaussian component
B
Nup133-RITE (14 h)
Spc42-mCherry
2 µm
Fraction in population
Distance SPB-NPC µm

# Fig. 2:

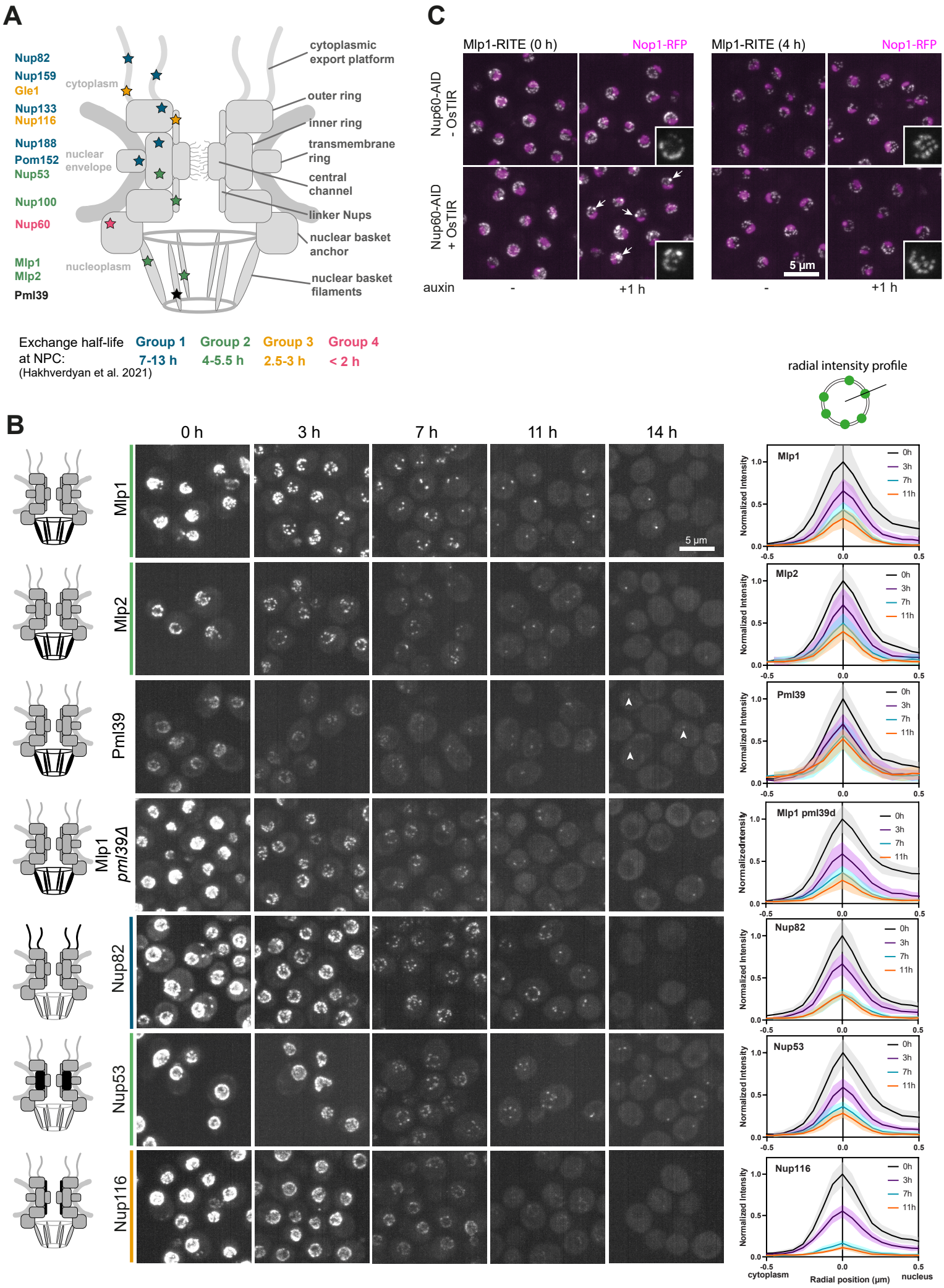
A
Nup82
Nup159
Gle1
Nup133
Nup116
Nup188
Pom152
Nup53
Nup100
Nup60
Mlp1
Mlp2
Pml39
cytoplasm
nuclear envelope
nucleoplasm
cytoplasmic export platform
outer ring
inner ring
transmembrane ring
central channel
linker Nups
nuclear basket anchor
nuclear basket filaments
Exchange half-life at NPC:
(Hakhverdyan et al. 2021)
Group 1 7-13 h
Group 2 4-5.5 h
Group 3 2.5-3 h
Group 4 < 2 h
C
Mlp1-RITE (0 h)
Nop1-RFP
Mlp1-RITE (4 h)
Nop1-RFP
Nup60-AID - OsTIR
Nup60-AID + OsTIR
5 µm
auxin
-
+1 h
-
+1 h
radial intensity profile
B
0 h
3 h
7 h
11 h
14 h
Mlp1
Mlp2
Pml39
Mlp1 pml39Δ
Nup82
Nup53
Nup116
5 µm
Normalized Intensity
0h
3h
7h
11h
Mlp1 pml39d
cytoplasm
Radial position (µm)
nucleus

Fig. S2:

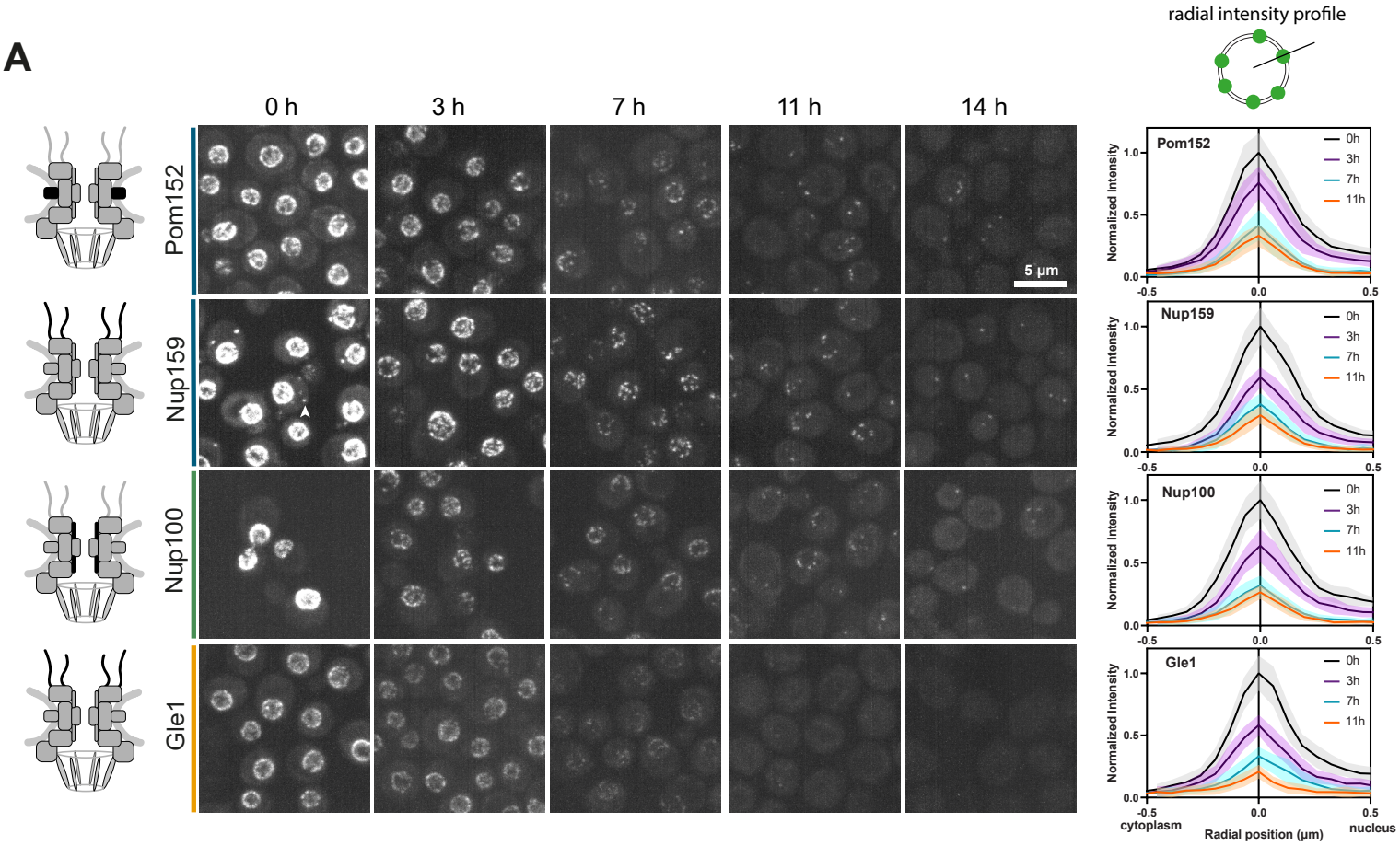
A
radial intensity profile
0 h
3 h
7 h
11 h
14 h
Pom152
Nup159
Nup100
Gle1
5 µm
Normalized Intensity
0h
3h
7h
11h
cytoplasm
Radial position (µm)
nucleus

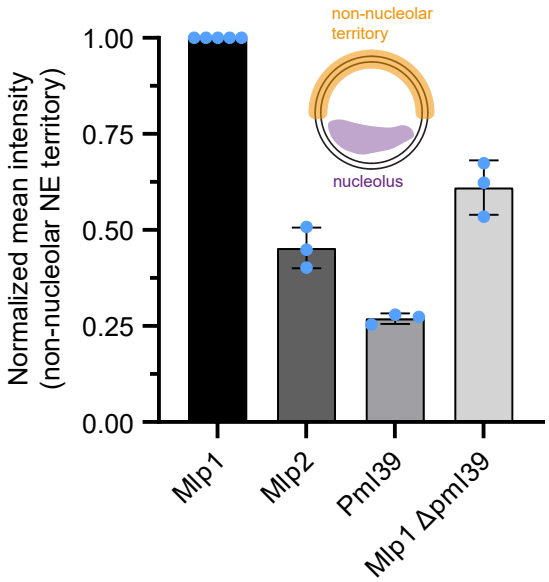
B
Normalized mean intensity
(non-nucleolar NE territory)
1.00
0.75
0.50
0.25
0.00
non-nucleolar
territory
nucleolus
Mlp1
Mlp2
Pml39
Mlp1 Δpml39

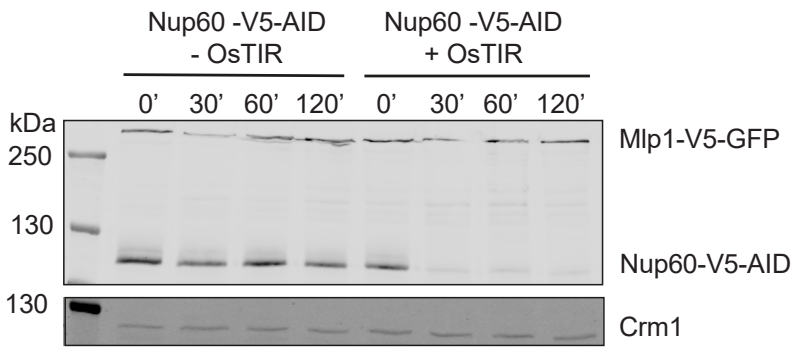
C
Nup60 -V5-AID
- OsTIR
Nup60 -V5-AID
+ OsTIR
0'
30'
60'
120'
kDa
250
130
130
Mlp1-V5-GFP
Nup60-V5-AID
Crm1

Fig. 3

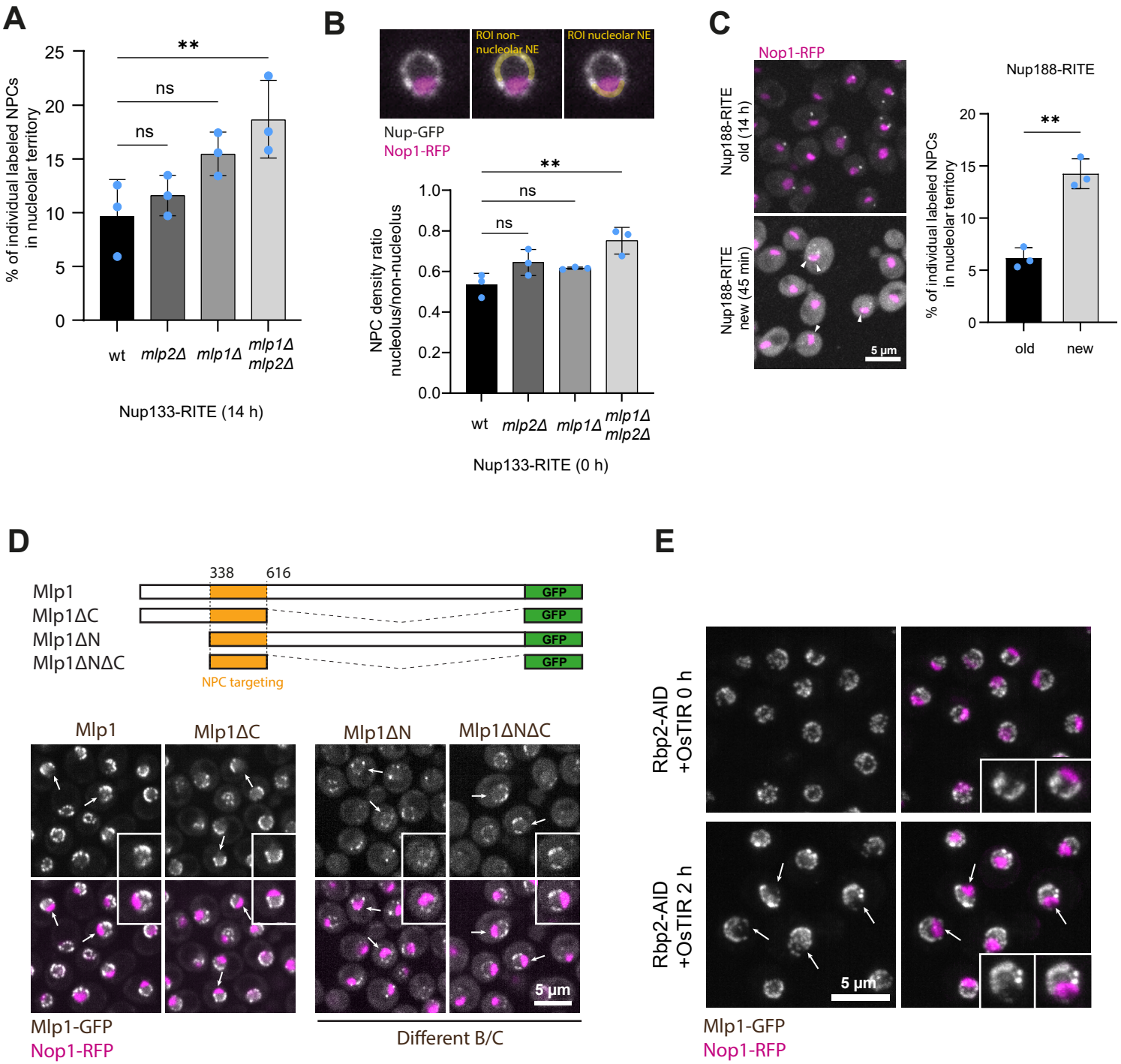
A
% of individual labeled NPCs in nucleolar territory
25
20
15
10
5
0
**
ns
ns
wt
mlp2Δ
mlp1Δ
mlp1Δ mlp2Δ
Nup133-RITE (14 h)
B
ROI non-nucleolar NE
ROI nucleolar NE
Nup-GFP
Nop1-RFP
NPC density ratio nucleolus/non-nucleolus
1.0
0.8
0.6
0.4
0.2
0.0
**
ns
ns
wt
mlp2Δ
mlp1Δ
mlp1Δ mlp2Δ
Nup133-RITE (0 h)
C
Nop1-RFP
Nup188-RITE old (14 h)
Nup188-RITE new (45 min)
5 µm
Nup188-RITE
% of individual labeled NPCs in nucleolar territory
20
15
10
5
0
**
old
new
D
338
616
Mlp1
Mlp1ΔC
Mlp1ΔN
Mlp1ΔNΔC
GFP
NPC targeting
Mlp1
Mlp1ΔC
Mlp1ΔN
Mlp1ΔNΔC
5 µm
Mlp1-GFP
Nop1-RFP
Different B/C
E
Rbp2-AID +OsTIR 0 h
Rbp2-AID +OsTIR 2 h
5 µm
Mlp1-GFP
Nop1-RFP

Fig. S3

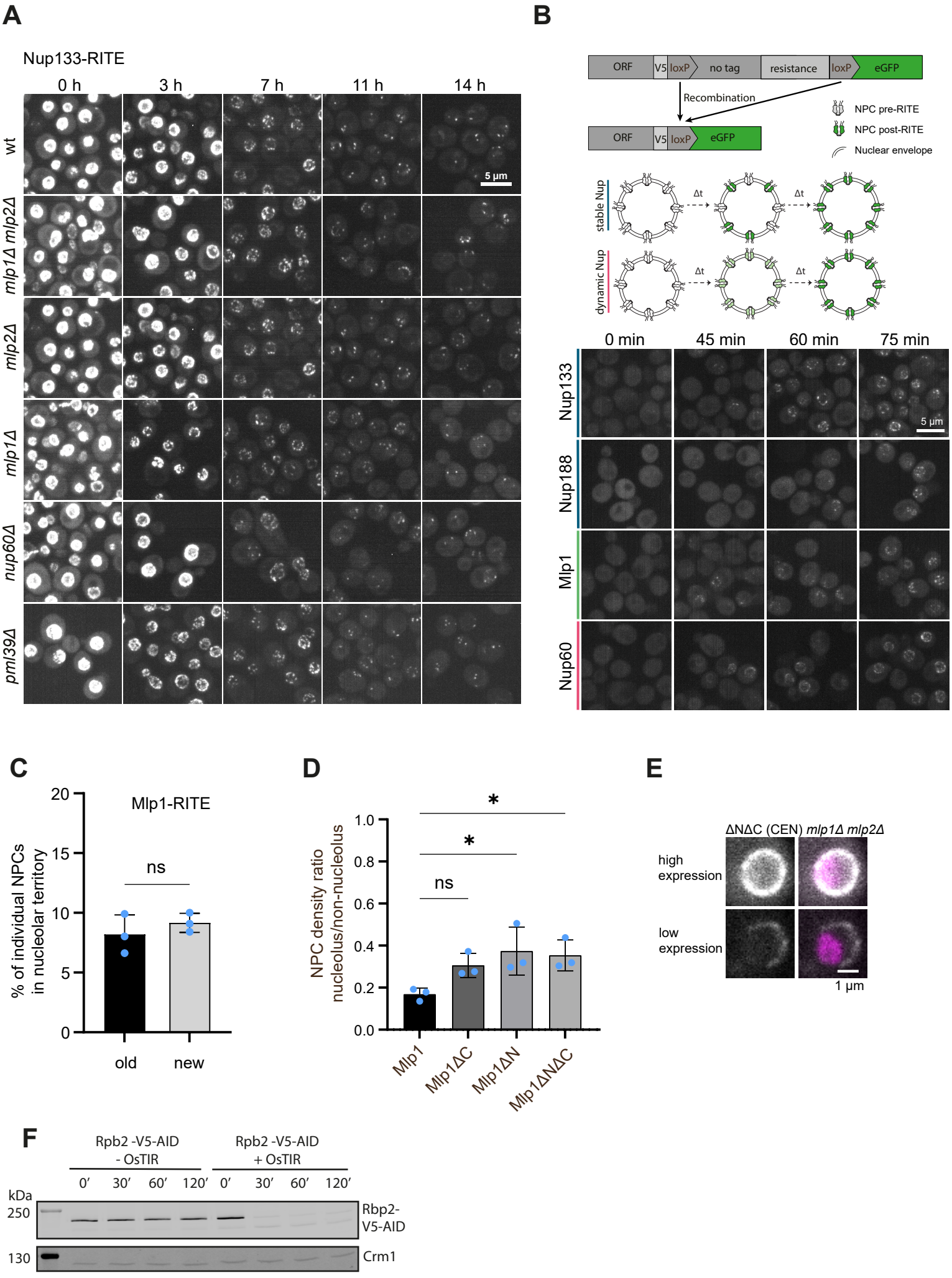
A
Nup133-RITE
0 h
3 h
7 h
11 h
14 h
wt
mlp1Δ mlp2Δ
mlp2Δ
mlp1Δ
nup60Δ
pml39Δ
5 µm
B
ORF
V5
loxP
no tag
resistance
loxP
eGFP
Recombination
ORF
V5
loxP
eGFP
NPC pre-RITE
NPC post-RITE
Nuclear envelope
stable Nup
dynamic Nup
Δt
0 min
45 min
60 min
75 min
Nup133
Nup188
Mlp1
Nup60
5 µm
C
Mlp1-RITE
% of individual NPCs in nucleolar territory
ns
old
new
D
NPC density ratio nucleolus/non-nucleolus
*
*
ns
Mlp1
Mlp1ΔC
Mlp1ΔN
Mlp1ΔNΔC
E
ΔNΔC (CEN) mlp1Δ mlp2Δ
high expression
low expression
1 µm
F
Rpb2 -V5-AID - OsTIR
Rpb2 -V5-AID + OsTIR
0′
30′
60′
120′
0′
30′
60′
120′
kDa
250
130
Rbp2-V5-AID
Crm1

Fig. 4

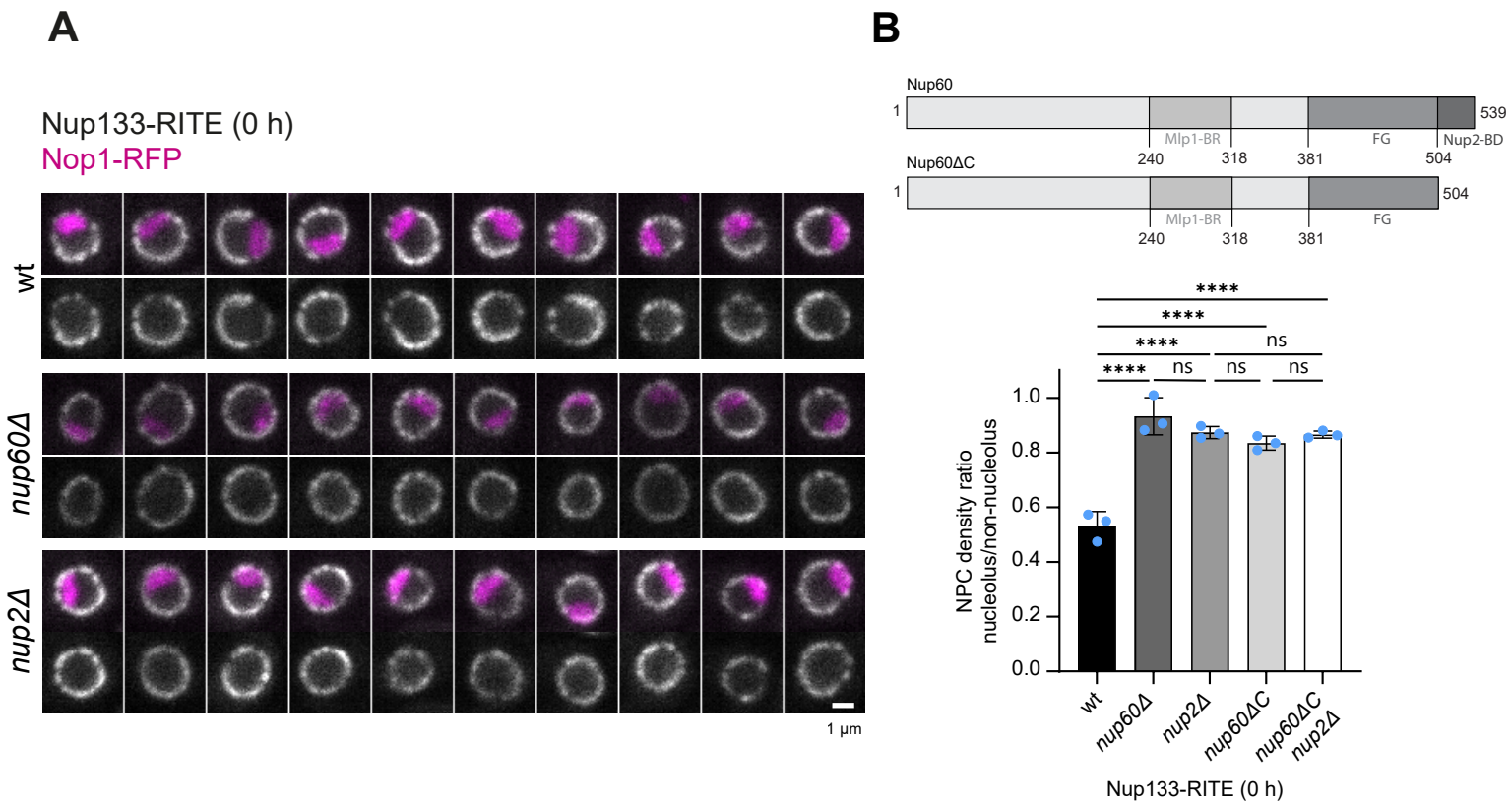
A
Nup133-RITE (0 h)
Nop1-RFP
wt
nup60Δ
nup2Δ
1 µm
B
Nup60
1
539
Mlp1-BR
FG
Nup2-BD
240
318
381
504
Nup60ΔC
1
504
Mlp1-BR
FG
240
318
381
****
****
****
ns
****
ns
ns
ns
NPC density ratio
nucleolus/non-nucleolus
1.0
0.8
0.6
0.4
0.2
0.0
wt
nup60Δ
nup2Δ
nup60ΔC
nup60ΔC
nup2Δ
Nup133-RITE (0 h)

Fig. S4

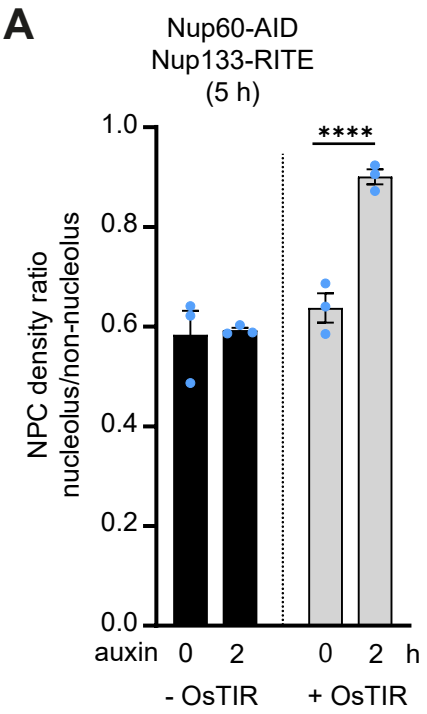
A
Nup60-AID
Nup133-RITE
(5 h)
NPC density ratio
nucleolus/non-nucleolus
1.0
0.8
0.6
0.4
0.2
0.0
****
auxin 0 2 0 2 h
- OsTIR
+ OsTIR

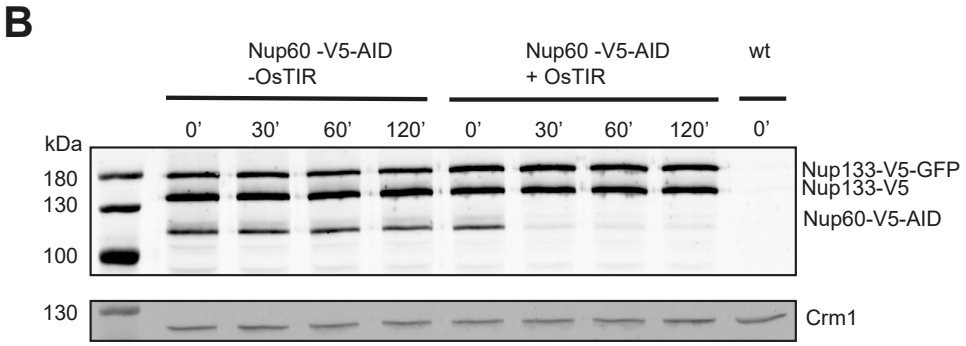
B
Nup60 -V5-AID
-OsTIR
Nup60 -V5-AID
+ OsTIR
wt
0' 30' 60' 120' 0' 30' 60' 120' 0'
kDa
180
130
100
130
Nup133-V5-GFP
Nup133-V5
Nup60-V5-AID
Crm1

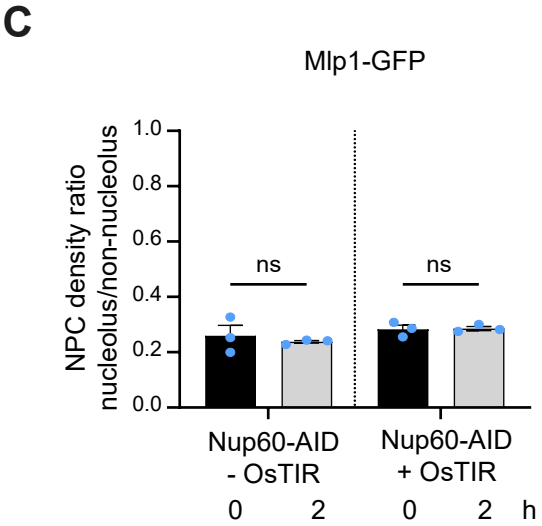
C
Mlp1-GFP
NPC density ratio
nucleolus/non-nucleolus
1.0
0.8
0.6
0.4
0.2
0.0
ns
ns
Nup60-AID
- OsTIR
Nup60-AID
+ OsTIR
0 2 0 2 h

Fig. 5:

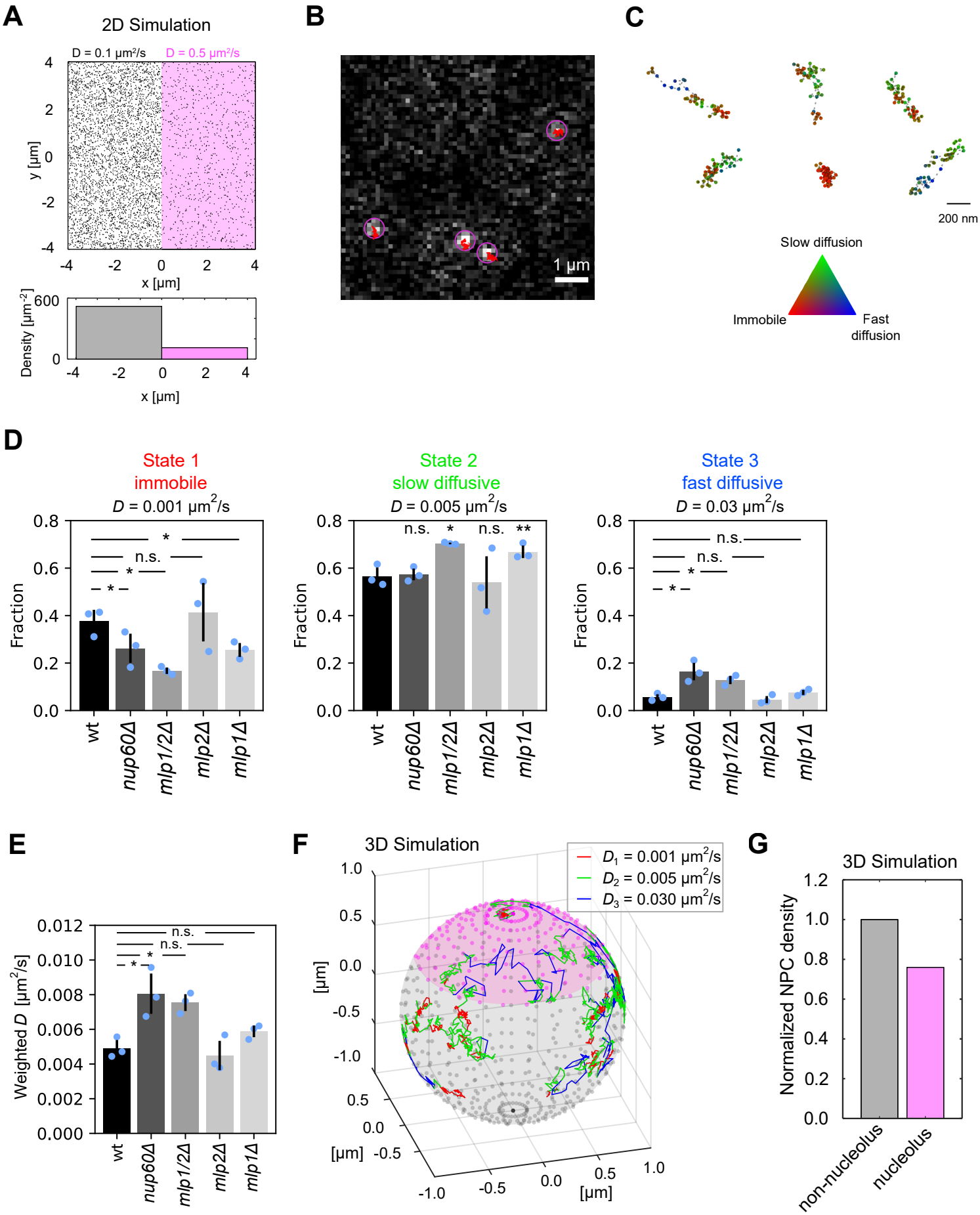
A
2D Simulation
D = 0.1 μm²/s
D = 0.5 μm²/s
y [μm]
x [μm]
Density [μm⁻²]
B
1 μm
C
200 nm
Slow diffusion
Immobile
Fast diffusion
D
State 1
immobile
D = 0.001 μm²/s
State 2
slow diffusive
D = 0.005 μm²/s
State 3
fast diffusive
D = 0.03 μm²/s
Fraction
n.s.
wt
nup60Δ
mlp1/2Δ
mlp2Δ
mlp1Δ
E
Weighted D [μm²/s]
F
3D Simulation
D1 = 0.001 μm²/s
D2 = 0.005 μm²/s
D3 = 0.030 μm²/s
[μm]
G
3D Simulation
Normalized NPC density
non-nucleolus
nucleolus

# Fig. S5:

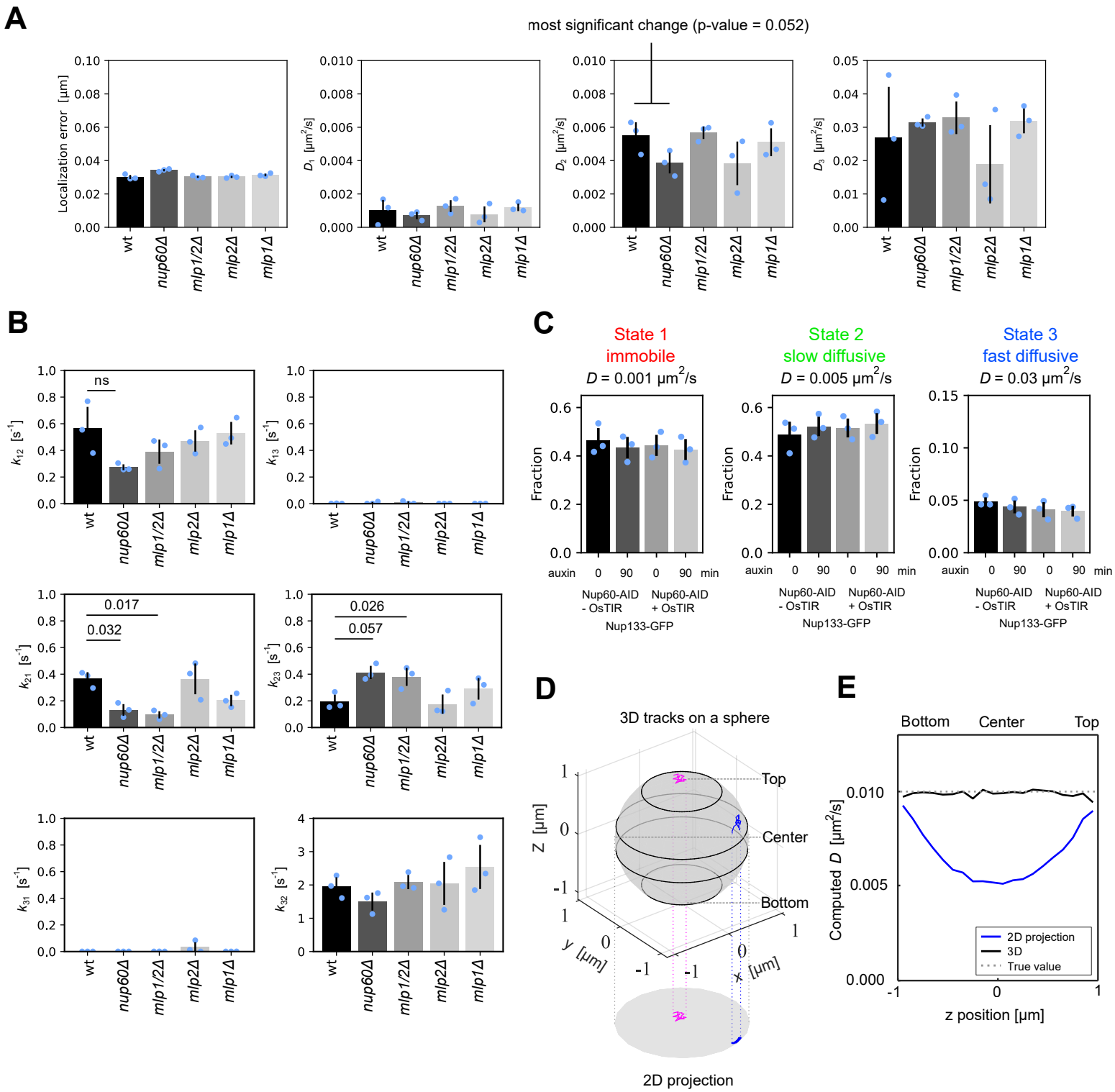
A
most significant change (p-value = 0.052)
Localization error [µm]
$D_1$ [µm²/s]
$D_2$ [µm²/s]
$D_3$ [µm²/s]
wt
nup60Δ
mlp1/2Δ
mlp2Δ
mlp1Δ
B
ns
0.017
0.032
0.026
0.057
$k_{12}$ [s⁻¹]
$k_{13}$ [s⁻¹]
$k_{21}$ [s⁻¹]
$k_{23}$ [s⁻¹]
$k_{31}$ [s⁻¹]
$k_{32}$ [s⁻¹]
C
State 1
immobile
D = 0.001 µm²/s
State 2
slow diffusive
D = 0.005 µm²/s
State 3
fast diffusive
D = 0.03 µm²/s
Fraction
auxin
0
90
0
90
min
Nup60-AID - OsTIR
Nup60-AID + OsTIR
Nup133-GFP
D
3D tracks on a sphere
Top
Center
Bottom
Z [µm]
y [µm]
x [µm]
2D projection
E
Bottom
Center
Top
Computed D [µm²/s]
2D projection
3D
True value
z position [µm]

# Fig. 6

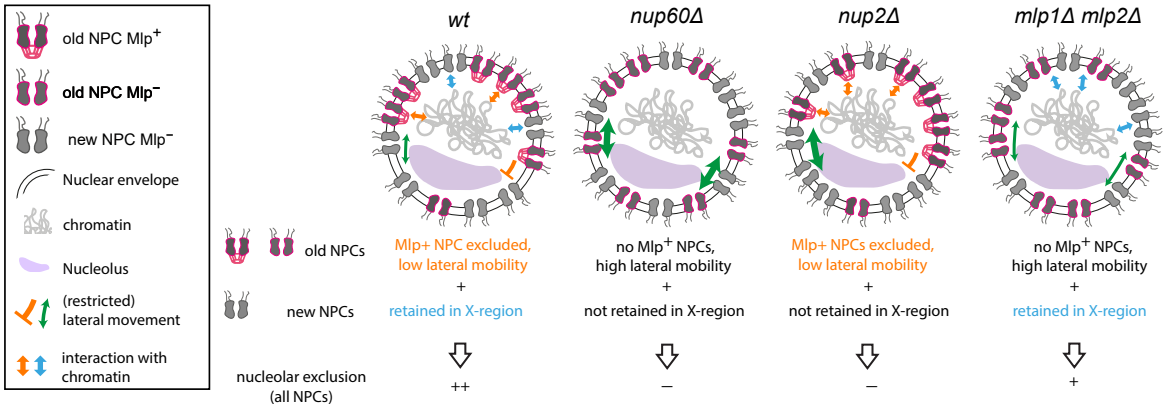
old NPC Mlp+
old NPC Mlp−
new NPC Mlp−
Nuclear envelope
chromatin
Nucleolus
(restricted) lateral movement
interaction with chromatin
wt
nup60Δ
nup2Δ
mlp1Δ mlp2Δ
old NPCs
new NPCs
Mlp+ NPC excluded, low lateral mobility
+
retained in X-region
no Mlp+ NPCs, high lateral mobility
+
not retained in X-region
Mlp+ NPCs excluded, low lateral mobility
+
not retained in X-region
no Mlp+ NPCs, high lateral mobility
+
retained in X-region
nucleolar exclusion (all NPCs)
++
–
–
+